nature physics

Article

https://doi.org/10.1038/s41567-026-03236-0

Laser-induced nucleation of magnetic hopfions

Received: 22 August 2025

Accepted: 2 March 2026

Published online: 21 April 2026

Check for updates

Xiaowen Chen[1,2], Donghai Yang[1], Zefang Li[3], Jiangteng Guo[3], Haixue Wang[3], Yue Hu[3], Vladyslav M. Kuchkin[4], Andrii S. Savchenko[5], Huai Zhang[6], Bei Ding[6], Zhipeng Hou[6], Wen Shi[2], Filipp N. Rybakov[7] ✉, Olle Eriksson[7,8], Stefan Blügel[5], Yu Han[2,9,10], Rafal E. Dunin-Borkowski[11], Nikolai S. Kiselev[5] ✉, Xuewen Fu[3,12,13] ✉ & Fengshan Zheng[1,2] ✉

Hopfions are three-dimensional topological solitons formed by closed loops of vortex strings, often taking the shape of rings. In magnetic crystals, hopfions have so far been observed only in unusual configurations in which hopfion rings are linked to skyrmion strings. Although theory predicts the existence of stable, isolated hopfions, their experimental realization has remained challenging. Here we demonstrate the laser-induced nucleation and direct observation of isolated magnetic hopfions in a cubic chiral magnet, FeGe, using transmission electron microscopy. The nucleation conditions are determined as a function of laser fluence and external magnetic field. Quantitative agreement between experimental data and micromagnetic simulations provides evidence for the emergence of isolated hopfions. We derive the topological invariant for hopfions under realistic rather than idealized boundary conditions and calculate its integer values for the observed objects. We also reveal that hopfions can coexist and interact with other topological spin textures over a broad field range. These findings demonstrate a contact-free approach for nucleating complex three-dimensional magnetic textures, thus providing a basis for further fundamental and applied research on magnetic hopfions.

Topological magnetic solitons are localized spin configurations that have properties such as those of classical particles[1]. Their nanoscale size, topological protection and high mobility make them promising candidates for next-generation spintronic and neuromorphic applications[2,3]. Chiral magnets are unique types of crystals in which competition between the Dzyaloshinskii–Moriya interaction (DMI), Heisenberg exchange and Zeeman energy gives rise to an extensive diversity of two-dimensional and three-dimensional (3D) topological solitons[4]. A prominent example of a two-dimensional topological soliton in magnetism is a skyrmion. In bulk crystals, skyrmions extend into the third dimension as filament-like structures known as skyrmion strings[5–7]. A hopfion can be thought of as a skyrmion string that is twisted and closed into a knotted loop. Such 3D solitons are characterized by a non-zero Hopf index and can exhibit a variety of configurations.

In frustrated magnets with competing exchange interactions[8–12], hopfions may exist in a ferromagnetic background. However, such hopfions remain experimentally unobserved. By contrast, chiral magnets with bulk-type DMIs support hopfions embedded in helical or conical spin modulations. In this case, the hopfions can form exotic composite configurations by linking with skyrmion strings to form structures that are referred to as hopfion rings on skyrmion strings. Such configurations have been observed experimentally in FeGe crystals[13].

Theory indicates that hopfions embedded in a helical background can exist as free-standing objects, which are sometimes referred to as heliknotons[14–16]. However, direct experimental observation of these solitons has remained an outstanding challenge. The difficulty stems from their metastable nature, as hopfions correspond to local minima in a complex energy landscape. For a system to relax into such a state,

A full list of affiliations appears at the end of the paper. ✉e-mail: philipp.rybakov@physics.uu.se; n.kiselev@fz-juelich.de; xwfu@nankai.edu.cn; zhengfs@scut.edu.cn

https://doi.org/10.1038/s41567-026-03236-0

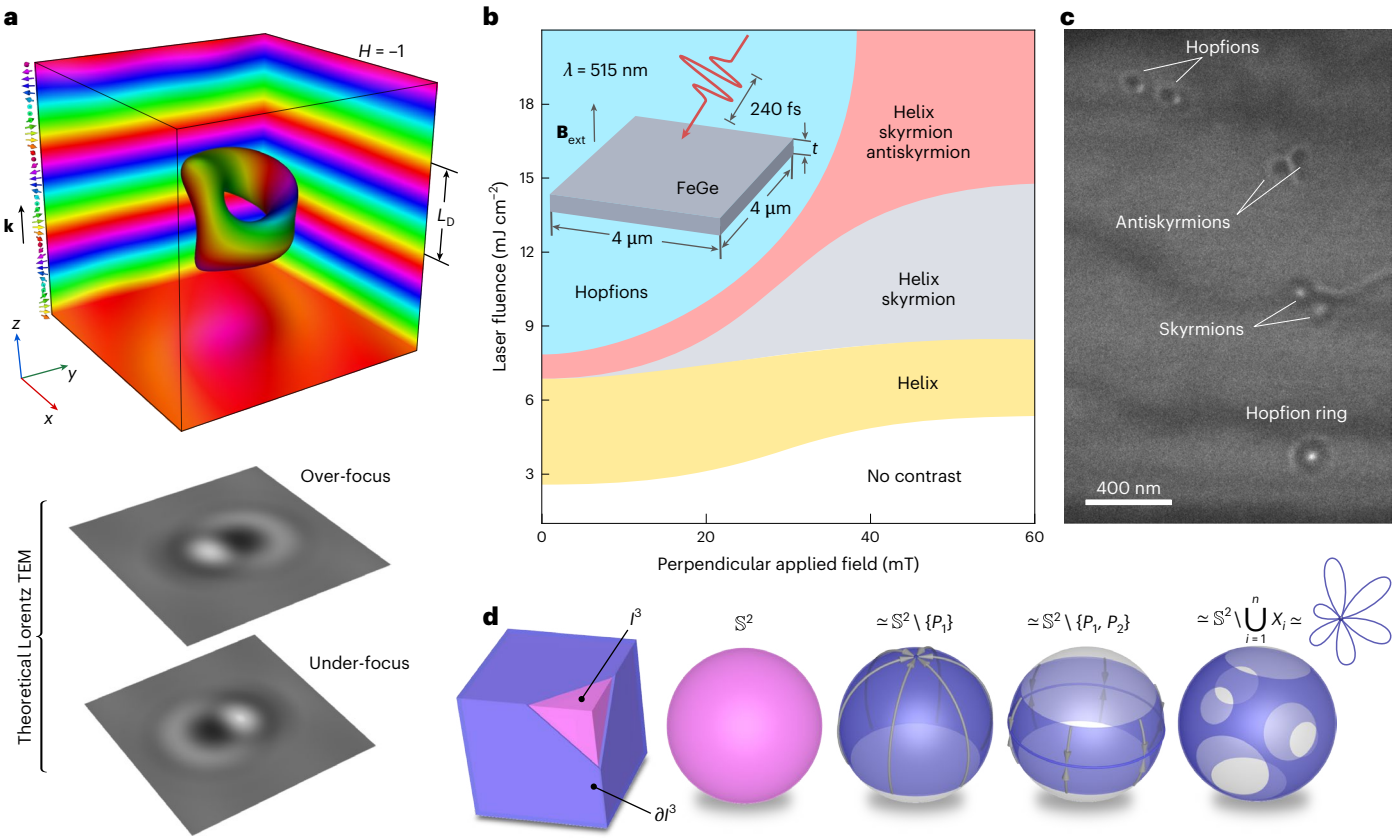

Fig. 1 | Hopfions in a background of helical spirals nucleated using ultrafast laser pulses. a, Top: statically stable solution of an isolated hopfion with Hopf index $H = -1$ in a plate of a chiral magnet with isotropic bulk DMI and zero external field. The hopfion is embedded in a helix with **k** vector perpendicular to the plate. The simulation domain is $3L_D$ in all directions, where L_D is the equilibrium period of the helix. Periodic boundary conditions are applied in the x–y plane. The magnetic texture is visualized at the domain boundaries and via the isosurface $m_z = -0.4$ within the volume, where m_z is the z component of the magnetization. Here and below, we use a standard colour code to indicate the direction of magnetization. White and black correspond to $m_z = +1$ and $m_z = -1$, respectively. The red-green-blue colour wheel encodes the in-plane orientation of the magnetization in the x–y plane. The two lower panels show theoretical Lorentz TEM images calculated in the over-focus and under-focus regimes for a defocus distance of 700 μm. **b**, Schematic representation of an experimental phase diagram of magnetic states nucleated by ultrafast laser pulses as a function of external magnetic field $\mathbf{B}_{ext}$ for an FeGe sample with a thickness $t = 110$ nm (Extended Data Fig. 3). Inset: schematic illustration of the set-up used in the TEM with in situ laser irradiation. The entire sample is irradiated by circularly polarized femtosecond laser pulses, resulting in the formation of topological spin textures. **c**, Representative over-focus Lorentz TEM image with a defocus distance of 700 μm showing a variety of topological magnetic solitons, including a pair of hopfions with $H = -1$ each as well as skyrmions and antiskyrmions nucleated by a single laser pulse under the conditions indicated in the blue region in **b**. **d**, Schematic visualization of relevant topological spaces. The first item is the cube I^3 with boundary ∂I^3, which can represent the localization domain of a hopfion depicted in **a**. The magenta sphere $\mathbb{S}^2$ illustrates the unconstrained order parameter space, indicating that the magnetization vector inside I^3 may take any arbitrary value on the sphere. The remaining blue spheres depict different constrained versions of the order parameter space on the boundary ∂I^3: $\mathbb{S}^2 \setminus \{P_1\}$, a sphere with one point removed; $\mathbb{S}^2 \setminus \{P_1, P_2\}$, a sphere with two punctures; $\mathbb{S}^2 \setminus \bigcup_{i=1}^{n} X_i$ (here $n = 7$), a sphere with several excluded regions. The latter space is homotopy-equivalent to a bouquet of $(n-1)$ circles.

it must overcome energy barriers that are difficult to surmount under standard experimental protocols. Although hopfion rings can be nucleated from edge modulations using carefully designed field sequences and sample geometries[13], the nucleation of isolated hopfions is even more demanding. In this work, we report a robust, contact-free method that can be used to nucleate and observe statically stable hopfions embedded in a helical background.

Recent advances in the ultrafast laser capabilities of the transmission electron microscope (TEM) have opened up new possibilities for the dynamic nucleation and manipulation of spin textures. Femtosecond laser pulses can excite magnetic systems on subpicosecond timescales by rapidly perturbing the electronic, spin and lattice degrees of freedom. Such transient processes can overcome the energy barriers that stabilize topological configurations, thereby enabling the laser-induced nucleation, transformation or annihilation of magnetic solitons, such as vortices[17–19] and skyrmions[20–29]. Compared with the use of other external stimuli, such as an electric current[30,31], magnetic field[13,32] or acoustic waves[33,34], optical excitation offers a contactless and energy-efficient approach for exciting magnetization dynamics. However, the optical nucleation and manipulation of 3D topological states, such as hopfions, remain largely unexplored. Here we demonstrate the efficient nucleation of hopfions in cubic chiral FeGe magnets using femtosecond laser pulses in the TEM.

Hopfion in a helical background

A representative example of a statically stable solution for an isolated hopfion embedded in a helical background is shown in Fig. 1a. Details of the micromagnetic simulation are provided in Methods. The hopfion is a continuous texture, even when it is embedded in the surrounding helical state. An analytical ansatz for this specific configuration is provided in Methods and in Extended Data Fig. 1. Note that the spin texture of this hopfion has no axial symmetry. As illustrated in Fig. 1a, theoretical Lorentz TEM images for this case also exhibit pronounced asymmetry[15]. Such characteristic contrast allows one to distinguish hopfions from other magnetic textures. In the literature, one can find claims that hopfions supposedly exist only within a ferromagnetic

phase. Using algebraic topology, we demonstrate below that this is by no means a necessary condition.

To classify a 3D topological magnetic texture, we apply methods from algebraic topology[35] and consider continuous maps between pairs of spaces:

$$f : (I^3, \partial I^3) \to (A, B), \tag{1}$$

where I^3 is the localization domain of the magnetic texture (taken here as a cube) and ∂I^3 is its boundary, as illustrated in Fig. 1d. The cube I^3 can be replaced by any homeomorphic domain, such as a ball, a cuboid or even the entire space $\mathbb{R}^3$. In the latter case, ∂I^3 corresponds to points at infinity. The target spaces A and B represent the order parameter inside the domain and on its boundary, respectively. Mapping (1) identifies homotopy classes that form the so-called third relative homotopy group of A modulo B. In the present case, the order parameter is the normalized magnetization field, $\mathbf{m}(\mathbf{r}) = \mathbf{M}/|\mathbf{M}|$, which takes values on a two-sphere, so $A = \mathbb{S}^2$. The space B represents a subspace of $\mathbb{S}^2$ determined by the constraints—boundary conditions—imposed on $\mathbf{m}(\mathbf{r} \in \partial I^3)$. If no constraints are imposed ($B = A$), then the relative homotopy group is trivial for any A: $\pi_3(A, A) = 0$, where π_3 is a homotopy group. This formalizes the intuitive fact that, without boundary restrictions, any texture can be continuously removed by translation across the boundary. Non-trivial topology, therefore, requires a constraint on certain magnetization directions on the boundary.

Numerous earlier studies on hopfions considered idealized yet maximally restrictive boundary conditions such that only a single spin direction was permitted at the boundary. That is, the subspace B reduces to a single point, $B = \mathbf{m}_0$ (refs. 1,8–10,36–40). In this case, the surrounding vacuum is a collinear magnetic phase, and the relative homotopy group reduces to the well-known equality: $\pi_3(\mathbb{S}^2, \mathbf{m}_0) \equiv \pi_3(\mathbb{S}^2) = \mathbb{Z}$. However, simple observation immediately allows one to substantially soften the restrictions on the boundary. Indeed, as the sphere with one point removed is contractible (it can be continuously shrunk to a point), then replacing $B = \mathbf{m}_0$ by $B = \mathbb{S}^2 \backslash \{P_1\}$ does not affect the homotopy classification. The central theoretical result of this work is that this statement can be generalized as follows. The third relative homotopy group of a sphere and a sphere with holes is isomorphic to the group of integers:

$$\pi_3\left(\mathbb{S}^2, \mathbb{S}^2 \backslash \bigcup_{i=1}^{n} X_i\right) = \mathbb{Z},\ n \geq 1, \tag{2}$$

where X_i are arbitrary disjoint simple regions ('holes') on the sphere. For the derivation of equation (2), see Methods. This result holds regardless of the shapes of X_i and shows that a non-trivial Hopf invariant exists under much weaker boundary restrictions than previously assumed. It is worth emphasizing that the second relative homotopy group for the same spaces, $\pi_2(\mathbb{S}^2, \mathbb{S}^2 \backslash \bigcup_{i=1}^{n} X_i)$, which classifies merons and skyrmions, is substantially different, as it depends on the number of holes and may even be non-abelian[41].

To illustrate the practical use of equation (2), consider a surrounding magnetization state that excludes a few discrete 'hard' directions of $\mathbf{m}$ corresponding to highly energetically unfavourable configurations. A hopfion embedded in a helical background is an example of this case where the subspace B is a two-punctured sphere, $\mathbb{S}^2 \backslash \{P_1, P_2\}$, or its homotopy equivalence, like a circle $\mathbb{S}^1$ or a spherical segment. In Fig. 1a, the helical phase surrounding the hopfion projects onto a spin sphere as a circle, although minor distortions make it resemble a spherical segment. The two punctures correspond to the most unfavourable deviations from the ideal helical phase, and they lie along the helix axis at $m_z = 1$ and $m_z = -1$. Under this constraint, B is homeomorphic to a sphere with its poles removed, $\mathbb{S}^2 \backslash \{P_1, P_2\}$, as shown schematically in Fig. 1d. Thus, this situation corresponds to the particular case of equation (2) with $n = 2$.

Isolated hopfions classified by equation (2) are naturally related to the abelian group $\mathbb{Z} \times \mathbb{Z}$ used to classify skyrmion–hopfion combinations[13] via the subgroup $\{0\} \times \mathbb{Z}$. In other words, a hopfion that is not linked to skyrmion strings can be characterized by a single integer H, usually referred to as hopfion charge. Moreover, isolated hopfions with $|H| = 1$ can be considered as (anti)generators. Supplementary Video 1 illustrates an example of a homotopy showing the unwinding of a hopfion ring by a heliknoton. The example corresponds to the following arithmetic of topological invariants: $(Q, H) = (-1, 1) + (0, -1) = (-1, 0)$, where Q denotes the skyrmion charge. The topological index of the hopfion depicted in Fig. 1a is $H = -1$. The detailed procedure for computing the Hopf index is outlined in Methods.

Hopfion laser nucleation

In our experiment, we used a set of plates fabricated via focused ion beam (FIB) milling from a single crystal of B20-type FeGe (Methods). The plate thicknesses t ranged from 110 nm to 200 nm, corresponding to ~$1.5L_D$ to $2.8L_D$, where L_D is the equilibrium period of the helix, as shown in Fig. 1a. Electron diffraction patterns recorded from samples of different thickness are shown in Extended Data Fig. 2a–d. Despite slight variations in crystallographic orientation relative to the sample normal, none of the samples was aligned along high-symmetry directions. Nevertheless, their magnetic behaviour and Lorentz TEM contrast are nearly identical. Thus, consistent with previous studies[6,7,13,42], B20-type FeGe can be regarded as a nearly isotropic system. A schematic illustration of the experimental set-up is shown in the inset of Fig. 1b. The femtosecond laser was circularly polarized. It had a wavelength of 515 nm, a spot diameter of 50 μm and a pulse duration of 240 fs. The laser fluence was tunable between 0 mJ cm^{-2} and 40 mJ cm^{-2}. During laser excitation, an external magnetic field of between 0 mT and ±100 mT was applied perpendicular to the plate. All measurements were performed at temperatures of between 95 K and 200 K.

Even a single femtosecond laser pulse was found to be sufficient to generate a rich variety of topological spin textures, including hopfions. However, for a given film thickness and temperature, efficient nucleation required the laser fluence and external magnetic field to fall within an optimal range. To identify the most favourable conditions for hopfion formation, the observed spin configurations were mapped systematically onto a state diagram as a function of laser fluence and applied magnetic field. Such a schematic diagram is shown in Fig. 1b for a 110-nm-thick FeGe plate. For an experimentally measured diagram of states after laser excitation, see Extended Data Fig. 3. The greatest diversity of spin textures is present at lower magnetic fields ($|\mathbf{B}_{ext}| \lesssim 35$ mT) and at laser fluences above 9 mJ cm^{-2}. A representative example of the resulting textures is shown in Fig. 1c. The figure shows a pair of hopfions at the top, antiskyrmions and skyrmions in the middle, and a hopfion ring on a single skyrmion string at the bottom. As a result of the high quality of the crystal, we did not observe preferable sites for hopfion nucleation. Instead, hopfions nucleated at random positions after each pulse. Theoretically calculated Lorentz TEM images of hopfions shown in Fig. 1a exhibit good agreement with the experimentally observed contrast.

Figure 2 shows a series of images of the phase shift recorded using off-axis electron holography. The images were acquired in zero external magnetic field with different angles between the plate normal and the incident electron beam direction. The line profiles shown in Fig. 2c–e demonstrate quantitative agreement between theoretical predictions and the experimental measurements. The images also illustrate a unique characteristic of hopfion contrast, which arises from its complex 3D structure. At lower sample tilt angles, the contrast comprises one bright and one dark spot. However, at the highest positive and negative sample tilt angles, it shows a pair of dark spots and a pair of bright spots, respectively. Extended Data Fig. 4 shows experimental and simulated Lorentz TEM tilt series for an isolated hopfion tilted about different axes, which further confirms the consistency between theory and experiment.

https://doi.org/10.1038/s41567-026-03236-0

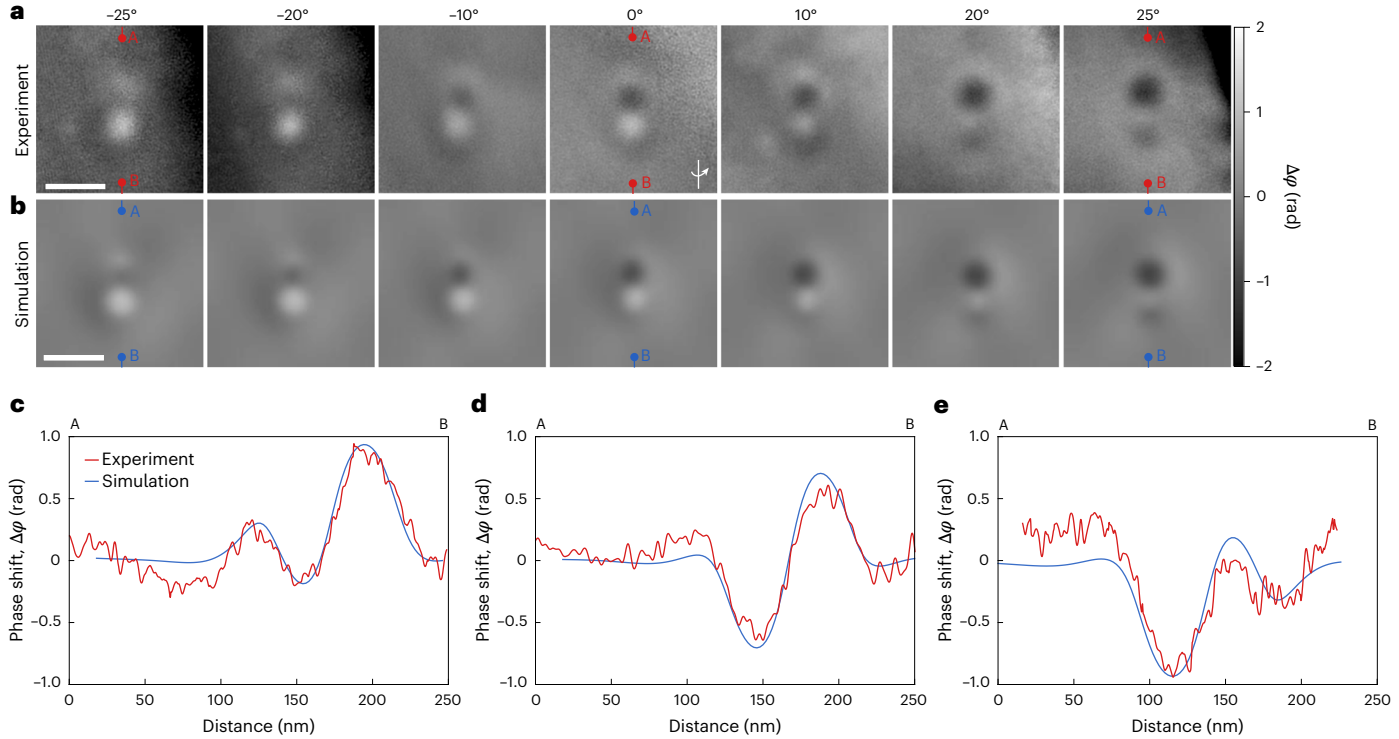

Fig. 2 | Tilt series of the quantitative phase shift of hopfions. a, Images of the experimental phase shift of an isolated hopfion recorded using off-axis electron holography as a function of sample tilt angle. The tilt axis is vertical, as marked on the zero-tilt image. The images were recorded for a 130-nm-thick sample at a temperature of 95 K in zero applied magnetic field. **b**, Corresponding simulated phase shifts. The simulations were performed for domains of size 300 nm × 300 nm × 130 nm. All experimental and simulated images of the phase shift have identical scale bars of 100 nm and are shown using the same greyscale, as indicated by the bar on the rightmost side of **a** and **b**. **c**–**e**, Line profiles extracted from the experimental (red) and simulated (blue) phase shift images for sample tilt angles of −25° (**c**), 0° (**d**) and +25° (**e**). The profiles were extracted between the marked points A and B.

Extended Data Fig. 5 compares the contrast of a hopfion with that of other particle-like states that are stable under similar conditions, namely, skyrmions, antiskyrmions and chiral bobbers. A comparative analysis of these images indicates that the experimental contrast originates from a hopfion and cannot be explained based on the other objects.

Before applying a laser pulse, the sample was usually saturated in a perpendicular magnetic field, which was then gradually reduced to zero. Under these conditions, the sample enters a helical (or conical) phase whose **k** vector is aligned perpendicular to the plate. Such a configuration produces no appreciable contrast in Lorentz TEM images. For an extended FeGe plate with easy-plane shape anisotropy[43], $\mathcal{K}_s = -\frac{1}{2}\mu_0 M_s^2$, where μ_0 is the vaccum permeability and M_s is the saturation magnetization, this configuration represents the ground state of the system. Therefore, saturation using a perpendicular magnetic field is, strictly speaking, not required before each laser pulse, as the system naturally tends towards this state. In earlier studies[6,7,13,42], the contribution of shape anisotropy was less pronounced because the lateral sample dimensions were much smaller, of the order of ~1 μm^2. By contrast, in the present work the plates are more extended, with lateral sizes of the order of tens of squared micrometres.

At lower laser fluences, the magnetic texture remains unchanged, irrespective of the applied magnetic field strength, and no further contrast appears after the laser pulse. Magnetic textures such as helical spirals, skyrmions and antiskyrmions appear only when the laser fluence exceeds a critical threshold value. (A representative example is shown in Supplementary Video 2 for the nucleation of hopfions by ultrafast laser pulses.) The blue region in Fig. 1b marks the regime that is optimal for the nucleation of hopfions. Skyrmions and antiskyrmions can also be nucleated under these conditions.

Figure 3 summarizes the hopfion and skyrmion nucleation probabilities for different applied magnetic fields, sample temperatures and sample thicknesses. Hopfion nucleation requires a higher laser fluence in the presence of a strong magnetic field and a lower fluence at elevated sample temperature, whereas skyrmion formation is promoted by increases in both magnetic field and temperature. The dependence on sample thickness was observed to be weak and non-monotonic, probably reflecting the finite penetration depth of the laser excitation and the reduced heating efficiency of thicker samples.

The observed dependence of magnetic texture nucleation on laser fluence indicates that heating is probably the dominant effect of laser excitation. In this regard, no other dependence on light polarization or repetition rate was observed. It is also important to note that, despite the nucleation of hopfions requiring a low magnetic field, their stability range is broad.

Hopfion stability diagram

Figure 4a shows a theoretically calculated stability diagram for hopfions embedded in a helix with the **k** vector perpendicular to the plate. An alternative configuration, in which the **k** vector lies in the plane of the sample, was considered earlier in ref. 16. The present diagram accounts for the effects of demagnetizing fields in an extended plate. The plate thickness and applied perpendicular magnetic field are expressed in both reduced units and real units corresponding to FeGe parameters (Methods).

Critical fields for hopfion collapse were calculated for two cases: with FIB-damaged surface layers[44] (red) and without such damage (blue). Based on previous estimates[13,44], we assumed a damaged layer thickness of 7 nm on each sample surface. Experimentally, the FIB-damaged surface layer was measured to have a thickness of 8 ± 2 nm (Extended Data Fig. 2e–k), in reasonable agreement with the value

https://doi.org/10.1038/s41567-026-03236-0

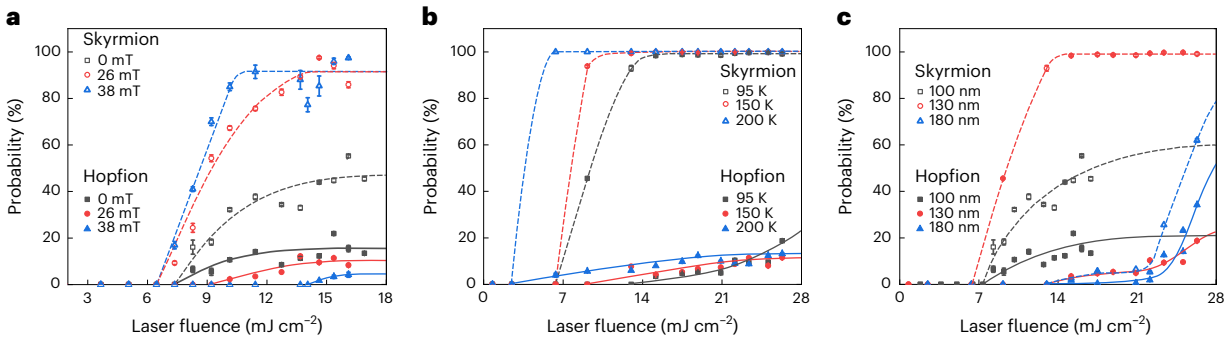

Fig. 3 | Probability of laser-induced hopfion nucleation. a–c, The probability of skyrmion nucleation is also shown for comparison. The sample was first saturated by a strong out-of-plane magnetic field and then exposed to a sequence of 1-Hz laser pulses. A similar process is illustrated in Supplementary Video 2. **a**, Nucleation probability in a 110-nm-thick sample for different applied magnetic fields at a fixed temperature of 95 K. **b**, Nucleation probability in a 130-nm-thick sample at different temperatures in zero applied magnetic field. **c**, Nucleation probability in samples of different thickness at a fixed temperature of 95 K in zero applied magnetic field. For each condition, at least 50 pulses were applied to each sample. The nucleation probability is defined as the fraction of pulses that produce at least one hopfion (or skyrmion). Error bars represent uncertainty in cases where the contrast cannot be characterized as a pure isolated hopfion or skyrmion due to the presence of adjacent textures. Including or excluding such ambiguous events provides upper and lower limits, respectively.

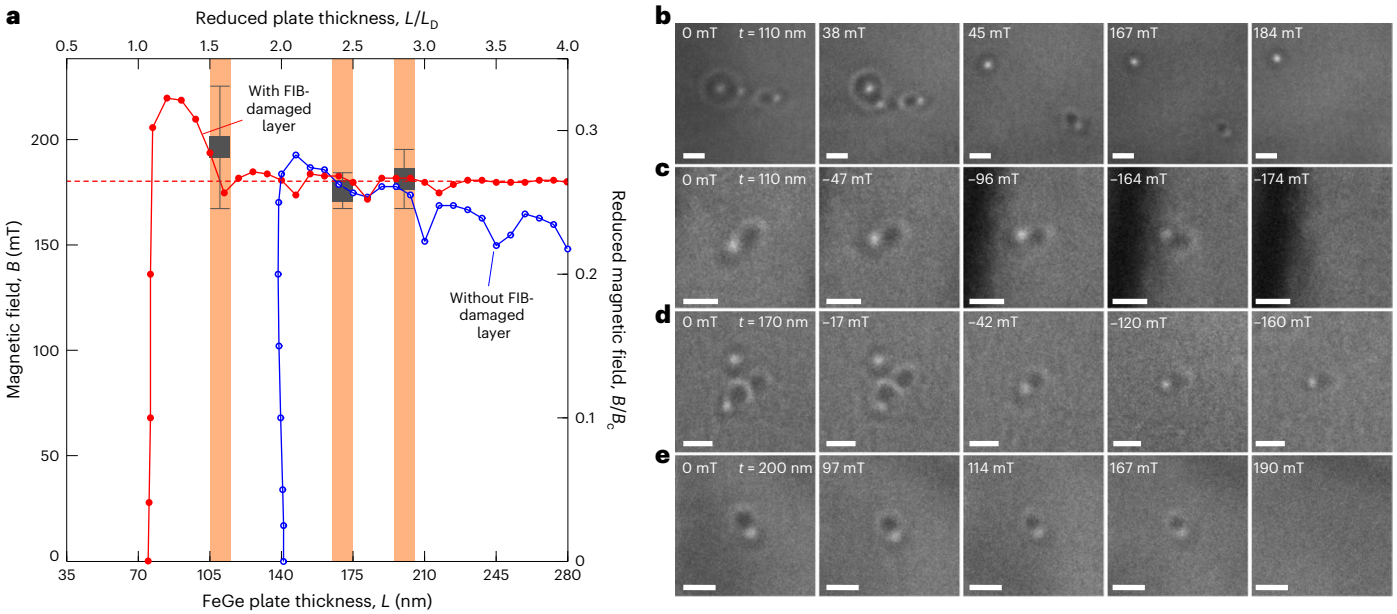

Fig. 4 | Stability of hopfions with $H = -1$ in thin plates. a, Theoretically calculated collapse field of isolated hopfions in an extended plate. The red line (solid circles) and blue line (hollow circles) correspond to cases with and without a 7-nm-thick FIB-damaged layer, respectively. The collapse field exhibits an oscillation with plate thickness, with a periodicity of approximately $\frac{1}{2} L_D$. The right axis indicates the external field in reduced units to the critical field, B_c, corresponding to the saturation field of the cone phase (Methods). The orange vertical bands mark approximate thicknesses of 110 ± 5 nm, 170 ± 5 nm and 200 ± 5 nm in the experimentally studied samples. The horizontal red dashed line marks the average collapse field of 180 mT for a wide range of plate thicknesses. The black squares denote experimentally measured collapse fields. Error bars indicate the range between the extreme values and the mean collapse field. For each thickness, collapse fields were extracted from three or four independent field-evolution events within the same sample. **b**,**c**, Series of Lorentz TEM images showing the in-field evolution of hopfions in a 110-nm-thick plate under positive (**b**) and negative (**c**) external magnetic fields. **d**,**e**, In-field evolution of a hopfion in 170-nm-thick (**d**) and 200-nm-thick (**e**) plates. Scale bars, 100 nm.

assumed in the calculations. Notably, the presence of a FIB-damaged layer substantially broadened the hopfion stability range. Without damage, the critical thickness for stability was ~140 nm, whereas with a damaged layer, it was ~75 nm. We attribute this difference to the presence of another surface barrier created by the damaged layer, which prevented hopfion escape at the sample surface.

The hopfion collapse field exhibited oscillatory behaviour with sample thickness, which is attributed to a chiral surface twist effect. Such oscillations reduced with increasing thickness and converged to a nearly constant value of about ~180 mT (horizontal dashed line). For a very thin plate, the collapse field could substantially deviate from this value to reach a value of up to ~220 mT.

The theoretical diagram is in good agreement with the experimental data. In particular, Fig. 4b,c shows Lorentz TEM images of isolated hopfions in a 110-nm-thick sample, and Fig. 4d,e shows hopfions in 170-nm-thick and 200-nm-thick samples as a function of applied magnetic field. Under-focus images corresponding to Fig. 4b–e are provided in Extended Data Fig. 6a–d. These results indicate that sample thickness does not markedly affect hopfion stability. This behaviour is consistent with the hopfion being a fully 3D magnetic object that is localized in all spatial directions. In agreement with the diagram, hopfion collapse is consistently observed at ~185 ± 10 mT. Other experimental data showing the in-field evolution of isolated hopfions are provided in Extended Data Figs. 7a and 8a and Supplementary Video 3.

https://doi.org/10.1038/s41567-026-03236-0

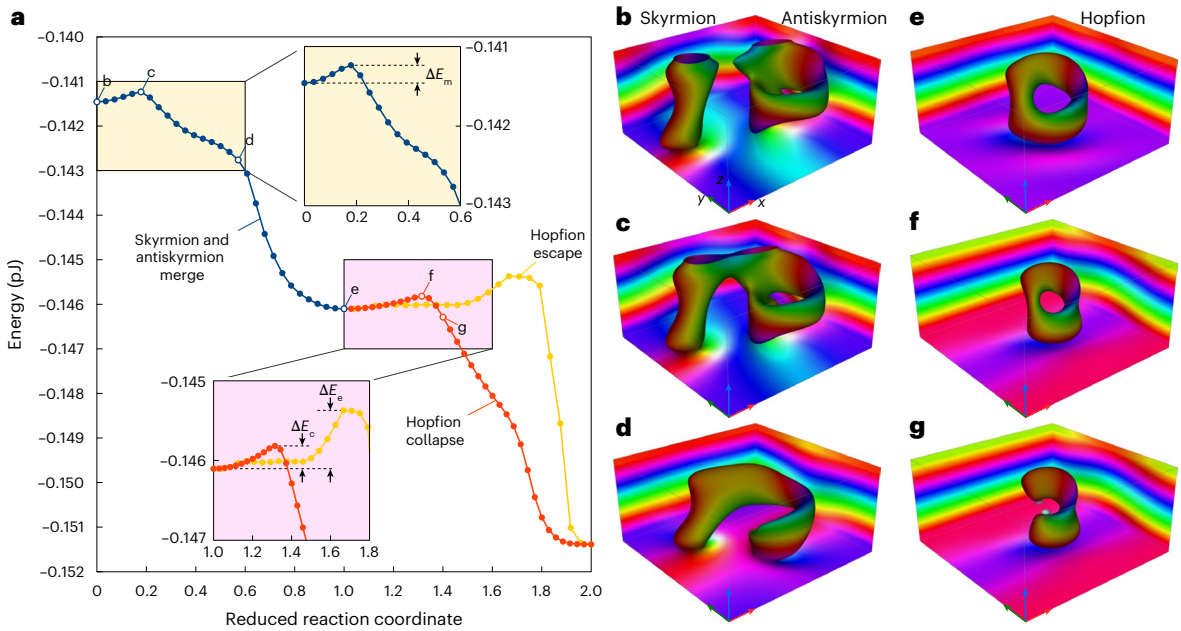

Fig. 5 | MEP for hopfion nucleation and annihilation. a, The MEP consists of two parts. The first part (blue) corresponds to the merger of a skyrmion–antiskyrmion pair into an isolated hopfion, and the second part (red) corresponds to the collapse of a hopfion into the conical phase. Each point represents the energy of a system configuration along the MEP, obtained using the RGNEB method. Insets: the energy barriers ΔE_m and ΔE_c. **b**–**g**, Snapshots of the system at selected points along the path, presented in the same format as Fig. 1a. The skyrmion–antiskyrmion pair (**b**) and hopfion (**e**) correspond to local energy minima. The configurations in **c** and **f** correspond to saddle points, and those in **d** and **g** correspond to intermediate states. The spherical isosurfaces in **g** mark the positions of Bloch points.

Furthermore, Extended Data Fig. 8d demonstrates the long-term temporal stability of a single hopfion, as it shows nearly constant Lorentz contrast over time.

Energy barriers for hopfion nucleation

To estimate the energy barriers and possible mechanisms for hopfion nucleation and annihilation, we calculated the minimum energy paths (MEPs)[45,46]. The MEPs shown in Fig. 5a are for an FeGe plate of thickness 105 nm in zero external field, assuming the same FIB-damaged layer as in the micromagnetic simulations (Methods). The vertical axis corresponds to the energy of the system, and the horizontal axis corresponds to the so-called reaction coordinate. The latter term describes the relative distance between distinct spin configurations in multi-dimensional geodesic space[45,46]. Points in the MEPs corresponding to values of the reduced reaction coordinate of 0 and 1 correspond to local energy minima of the system. They describe the stable skyrmion–antiskyrmion pair depicted in Fig. 5b and the hopfion depicted in Fig. 5e. A reduced reaction coordinate of 2 corresponds to the helical spiral state. Figure 5c,f shows snapshots of the system at the saddle points. Intermediate configurations are shown in Fig. 5d,g.

The MEP shown in Fig. 5a comprises two parts. The first part (blue) corresponds to the merger of a skyrmion–antiskyrmion pair into a hopfion. The second part corresponds to the collapse of a hopfion into the helical phase, which can follow two distinct pathways: collapse via hopfion shrinking (red) and hopfion escape through the free surface (yellow). Extended Data Fig. 9 shows these paths separately and includes further snapshots of intermediate configurations. When viewed in the reverse direction, that is, from the low energy to the high energy states, the first part can be thought of as a hopfion splitting into a skyrmion and an antiskyrmion, and the second part can be thought of as spontaneous hopfion nucleation in a helical background. Both processes are, of course, highly improbable due to the presence of very large energy barriers. Therefore, hopfion formation via the merger of a skyrmion–antiskyrmion pair seems to be the most plausible mechanism. Note that this transition was continuous, and no magnetic singularities appeared throughout the path. The energy barrier for the transition from a skyrmion–antiskyrmion pair into a hopfion, ΔE_m, is relatively low. Collapse of the hopfion is protected by slightly higher energy barriers, $\Delta E_c > \Delta E_m$. As a result, the probability for the transition from a skyrmion–antiskyrmion pair into a hopfion is expected to be higher than the probability for hopfion collapse. The above arguments are naturally applied for lower temperatures, $k_B T \lesssim \Delta E_c$, where k_B is the Boltzmann constant, and they agree with the experimental observations. Supplementary Video 4 illustrates hopfion nucleation from the merger of a skyrmion and an antiskyrmion, both experimentally and theoretically.

Composite textures with hopfions

Figure 4b illustrates a composite state, in which a hopfion is located next to a hopfion ring on a skyrmion string. Such a configuration is not unique. Our experiments reveal that femtosecond laser excitation can nucleate a wide diversity of composite textures, including hopfion clusters, hopfion–skyrmion pairs and hopfion–antiskyrmion pairs. Figure 6 illustrates such configurations and their in-field evolution. All the composite textures in Fig. 6 were nucleated in the absence of an external magnetic field. More examples of composite textures with hopfions are provided in Extended Data Figs. 7b,c and 8b–d.

The in-field evolution of such composite textures is, in general, consistent with the collapse field estimated for an isolated hopfion. However, for configurations in which a hopfion interacts with other magnetic textures, it often collapses at a slightly lower field. For example, in a hopfion pair (Fig. 6a), the first hopfion collapses at 167 mT, whereas the other hopfion couples to a skyrmion and then disappears at ~200 mT. In a hopfion–skyrmion pair (Fig. 6b), the hopfion collapses at 196 mT, whereas the adjacent skyrmion remains stable until ~500 mT. By contrast, in a hopfion–antiskyrmion pair (Fig. 6c), the antiskyrmion vanishes first at 108 mT, followed by hopfion annihilation at 132 mT. Under-focus images corresponding to Fig. 6 are provided in Extended Data Fig. 6e–h. These results indicate that the presence of magnetic inhomogeneities introduces local distortions, which lower the effective energy barrier for hopfion collapse.

https://doi.org/10.1038/s41567-026-03236-0

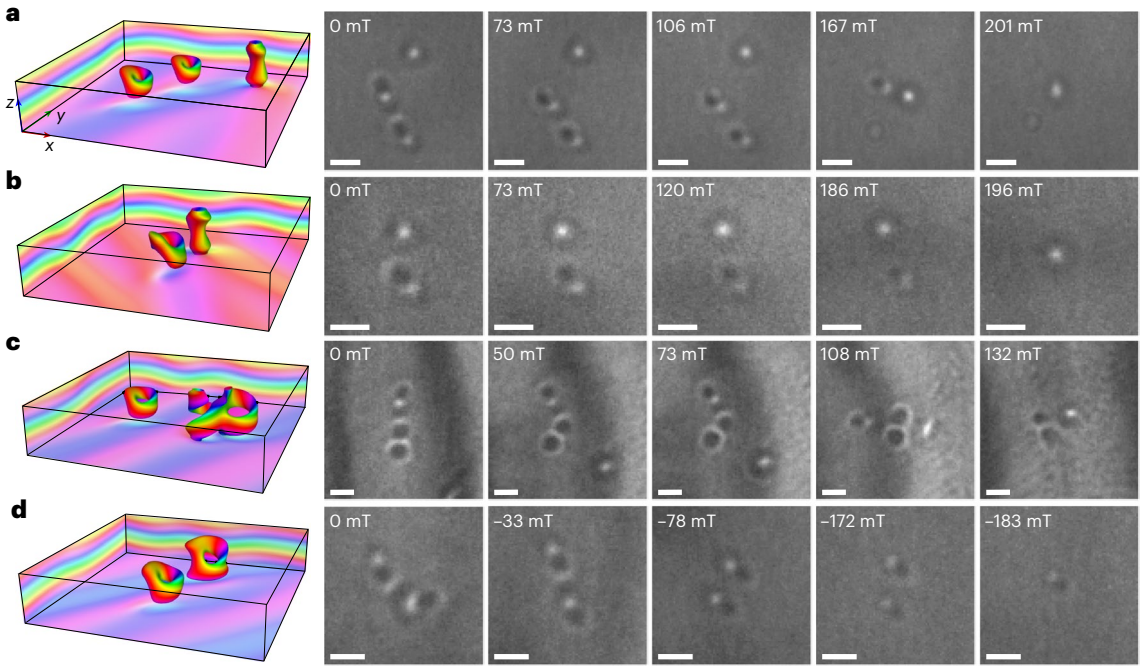

Fig. 6 | Evolution of hopfions in a perpendicular external magnetic field. **a**–**d**, The first column shows isosurfaces ($m_z = -0.5$) for different statically stable combinations of topological solitons, including a hopfion pair (**a** and **d**), a hopfion–skyrmion pair (**b**) and a hopfion–antiskyrmion pair (**c**). The simulations were performed in a domain of size 512 nm × 512 nm × 110 nm, with periodic boundary conditions applied in the x–y plane and a mesh of 256 × 256 × 55 cuboids. In **a**, the hopfions are aligned parallel and in **d** the hopfions are aligned vertically. Their field evolution is shown in the form of over-focus Lorentz TEM images in subsequent columns. The strength of the applied magnetic field is marked in the upper left corner of each image. The Lorentz TEM images were acquired at 95 K with a defocus of 700 µm. The sample thickness was 110 nm. Scale bars, 100 nm.

Note that the theoretical diagram shown in Fig. 4a is assumed to be symmetrical with respect to the direction of the applied perpendicular magnetic field. In other words, theory predicts that the most favourable hopfion state is at zero applied field. An increase in the strength of the perpendicular applied field in either direction should then lead to hopfion collapse at identical fields. This prediction is in full agreement with the experimental observations. When an external magnetic field is applied in the opposite direction (see, for example, Figs. 4c,d and 6d and Extended Data Fig. 7b), hopfions in all configurations annihilate at nearly the same values: −174 mT (isolated), −183 mT (hopfion pair), −189 mT (hopfion–skyrmion) and −130 mT (hopfion–antiskyrmion). Supplementary Videos 5, 6 and 7 show the field-sweep evolution for the hopfion–skyrmion, hopfion–antiskyrmion and hopfion–skyrmion–antiskyrmion configurations, respectively.

In addition to a perpendicular field, hopfion stability was also assessed for magnetic fields that were tilted by small angles of ~5–8°. Such a tilt can be interpreted as an another in-plane magnetic field applied to the sample (Extended Data Fig. 10). Hopfions are then expected to become more fragile and to collapse at lower fields, ~±55 mT. Nevertheless, in some measurements, hopfions survived up to 180 mT, even in the presence of tilted fields (Extended Data Fig. 10a).

The results presented here establish a magnetic-field-free and contactless approach for nucleating 3D topological solitons in a cubic chiral magnet, FeGe. This approach goes beyond the geometrically confined nanostructures studied in earlier works[13]. Furthermore, these results may lead to new concepts for spintronics based on other approaches for manipulating 3D magnetic textures with a laser beam.

During the review process, we became aware of a submitted manuscript reporting the electrical writing of heliknotons in chiral magnets[47]. This work demonstrates that magnetic hopfions can be nucleated and moved by electrical current pulses, which may be relevant for potential applications. Accordingly, this points to two complementary approaches to hopfion nucleation—current-induced nucleation and optical nucleation—introduced here.

Online content

Any methods, additional references, Nature Portfolio reporting summaries, source data, extended data, supplementary information, acknowledgements, peer review information; details of author contributions and competing interests; and statements of data and code availability are available at https://doi.org/10.1038/s41567-026-03236-0.

References

1. Kosevich, A. M., Ivanov, B. A. & Kovalev, A. S. Magnetic solitons. *Phys. Rep.* **194**, 117–238 (1990).
2. Fert, A., Reyren, N. & Cros, V. Magnetic skyrmions: advances in physics and potential applications. *Nat. Rev. Mater.* **2**, 17031 (2017).
3. Zhou, Y. et al. Topological spin textures: basic physics and devices. *Adv. Mater.* **37**, 2312935 (2025).
4. Tokura, Y. & Kanazawa, N. Magnetic skyrmion materials. *Chem. Rev.* **121**, 2857–2897 (2020).
5. Park, H. S. et al. Observation of the magnetic flux and three-dimensional structure of skyrmion lattices by electron holography. *Nat. Nanotechnol.* **9**, 337–342 (2014).
6. Du, H. et al. Interaction of individual skyrmions in a nanostructured cubic chiral magnet. *Phys. Rev. Lett.* **120**, 197203 (2018).
7. Zheng, F. et al. Magnetic skyrmion braids. *Nat. Commun.* **12**, 5316 (2021).
8. Bogolubsky, I. L. Three-dimensional topological solitons in the lattice model of a magnet with competing interactions. *Phys. Lett. A* **126**, 511–514 (1988).
9. Sutcliffe, P. Skyrmion knots in frustrated magnets. *Phys. Rev. Lett.* **118**, 247203 (2017).
10. Rybakov, F. N. et al. Magnetic hopfions in solids. *APL Mater.* **10**, 111113 (2022).

11. Liu, Y., Hou, W., Han, X. & Zang, J. Three-dimensional dynamics of a magnetic hopfion driven by spin transfer torque. *Phys. Rev. Lett.* **124**, 127204 (2020).
12. Zhang, Z. et al. Magnon scattering modulated by omnidirectional hopfion motion in antiferromagnets for meta-learning. *Sci. Adv.* **9**, eade7439 (2023).
13. Zheng, F. et al. Hopfion rings in a cubic chiral magnet. *Nature* **623**, 718–723 (2023).
14. Tai, J.-S. B. & Smalyukh, I. I. Three-dimensional crystals of adaptive knots. *Science* **365**, 1449–1453 (2019).
15. Voinescu, R., Tai, J.-S. B. & Smalyukh, I. Hopf solitons in helical and conical backgrounds of chiral magnetic solids. *Phys. Rev. Lett.* **125**, 057201 (2020).
16. Kuchikin, V. M. et al. Heliknoton in a film of cubic chiral magnet. *Front. Phys.* **11**, 1201018 (2023).
17. Eggebrecht, T. et al. Light-induced metastable magnetic texture uncovered by in situ Lorentz microscopy. *Phys. Rev. Lett.* **118**, 097203 (2017).
18. Fu, X. et al. Optical manipulation of magnetic vortices visualized in situ by Lorentz electron microscopy. *Sci. Adv.* **4**, eaat3077 (2018).
19. Silva, R. et al. Nanoscale mapping of ultrafast magnetization dynamics with femtosecond Lorentz microscopy. *Phys. Rev. X* **8**, 031052 (2018).
20. Finazzi, M. et al. Laser-induced magnetic nanostructures with tunable topological properties. *Phys. Rev. Lett.* **110**, 177205 (2013).
21. Je, S. et al. Creation of magnetic skyrmion bubble lattices by ultrafast laser in ultrathin films. *Nano Lett.* **18**, 7362–7371 (2018).
22. Berruto, G. et al. Laser-induced skyrmion writing and erasing in an ultrafast cryo-Lorentz transmission electron microscope. *Phys. Rev. Lett.* **120**, 117201 (2018).
23. Büttner, F. et al. Observation of fluctuation-mediated picosecond nucleation of a topological phase. *Nat. Mater.* **20**, 30–37 (2021).
24. Truc, B. et al. Light-induced metastable hidden skyrmion phase in the Mott insulator Cu_2OSeO_3. *Adv. Mater.* **35**, 2304197 (2023).
25. Khela, M. et al. Laser-induced topological spin switching in a 2D van der Waals magnet. *Nat. Commun.* **14**, 1378 (2023).
26. Li, Z. et al. Room-temperature sub-100 nm Néel-type skyrmions in non-stoichiometric van der Waals ferromagnet $Fe_{3-x}GaTe_2$ with ultrafast laser writability. *Nat. Commun.* **15**, 1017 (2024).
27. Kalin, J. et al. Optical creation and annihilation of skyrmion patches in a chiral magnet. *Phys. Rev. Appl.* **21**, 034065 (2024).
28. Titze, T. et al. All-optical control of bubble and skyrmion breathing. *Phys. Rev. Lett.* **133**, 156701 (2024).
29. Kern, L.-M. et al. Controlled formation of skyrmion bags. *Adv. Mater.* **37**, 2501250 (2025).
30. Wang, W. et al. Electrical manipulation of skyrmions in a chiral magnet. *Nat. Commun.* **13**, 1593 (2022).
31. Song, D. et al. Steady motion of 80-nm-size skyrmions in a 100-nm-wide track. *Nat. Commun.* **15**, 5614 (2024).
32. Liu, J. et al. Manipulation of skyrmion by magnetic field gradients: a Stern–Gerlach-like experiment. *Nano Lett.* **23**, 4931–4937 (2023).
33. Chen, R. et al. Ordered creation and motion of skyrmions with surface acoustic wave. *Nat. Commun.* **14**, 4427 (2023).
34. Yang, Y. et al. Acoustic-driven magnetic skyrmion motion. *Nat. Commun.* **15**, 1018 (2024).
35. Hatcher, A. *Algebraic Topology* (Cambridge Univ. Press, 2002).
36. Gladikowski, J. & Hellmund, M. Static solitons with nonzero Hopf number. *Phys. Rev. D* **56**, 5194–5199 (1997).
37. Faddeev, L. & Niemi, A. J. Stable knot-like structures in classical field theory. *Nature* **387**, 58–61 (1997).
38. Battye, R. A. & Sutcliffe, P. M. Knots as stable soliton solutions in a three-dimensional classical field theory. *Phys. Rev. Lett.* **81**, 4798 (1998).
39. Borrisov, A. B. & Rybakov. F. N. Stationary precession topological solitons with nonzero Hopf invariant in a uniaxial ferromagnet. *JETP Lett.* **88**, 264–267 (2008).
40. Kent, N. et al. Creation and observation of hopfions in magnetic multilayer systems. *Nat. Commun.* **12**, 1562 (2021).
41. Rybakov, F. N. et al. Topological invariants of vortices, merons, skyrmions, and their combinations in continuous and discrete systems. *Phys. Rev. B* **111**, 134417 (2025).
42. Zheng, F. et al. Skyrmion–antiskyrmion pair creation and annihilation in a cubic chiral magnet. *Nat. Phys.* **18**, 863–868 (2022).
43. Di Fratta, G. et al. Variational principles of micromagnetics revisited. *SIAM J. Math. Anal.* **52**, 3580–3599 (2020).
44. Yang, L. et al. Embedded skyrmion bags in thin films of chiral magnets. *Adv. Mater.* **36**, 2403274 (2024).
45. Bessarab, P. F. et al. Method for finding mechanism and activation energy of magnetic transitions, applied to skyrmion and antivortex annihilation. *Comput. Phys. Commun.* **196**, 335–347 (2015).
46. Bessarab, P. F. Comment on 'Path to collapse for an isolated Néel skyrmion'. *Phys. Rev. B* **95**, 136401 (2017).
47. Li, L. et al. Electrically writing a magnetic heliknoton in a chiral magnet. *Nat. Mater.* https://doi.org/10.1038/s41563-025-02450-0 (2026).

[1]Spin-X Institute, School of Physics and Optoelectronics, State Key Laboratory of Luminescent Materials and Devices, Guangdong-Hong Kong-Macao Joint Laboratory of Optoelectronic and Magnetic Functional Materials, South China University of Technology, Guangzhou, China. [2]Center for Electron Microscopy, South China University of Technology, Guangzhou, China. [3]Ultrafast Electron Microscopy Laboratory, The MOE Key Laboratory of Weak-Light Nonlinear Photonics, School of Physics, Nankai University, Tianjin, China. [4]Department of Physics and Materials Science, University of Luxembourg, Luxembourg, Luxembourg. [5]Peter Grünberg Institute, Forschungszentrum Jülich and JARA, Jülich, Germany. [6]Guangdong Provincial Key Laboratory of Optical Information Materials and Technology, Institute for Advanced Materials, South China Academy of Advanced Optoelectronics, South China Normal University, Guangzhou, China. [7]Department of Physics and Astronomy, Uppsala University, Uppsala, Sweden. [8]Wallenberg Initiative Materials

Science for Sustainability, Uppsala University, Uppsala, Sweden. [9]School of Emergent Soft Matter, South China University of Technology, Guangzhou, China. [10]State Key Laboratory of Pulp and Paper Engineering, South China University of Technology, Guangzhou, China. [11]Ernst Ruska-Centre for Microscopy and Spectroscopy with Electrons and Peter Grünberg Institute, Forschungszentrum Jülich, Jülich, Germany. [12]School of Materials Science and Engineering, Smart Sensing Interdisciplinary Science Center, Nankai University, Tianjin, China. [13]Academy for Advanced Interdisciplinary Studies, Nankai University, Tianjin, China. ✉e-mail: philipp.rybakov@physics.uu.se; n.kiselev@fz-juelich.de; xwfu@nankai.edu.cn; zhengfs@scut.edu.cn

Methods

Specimen preparation

FeGe TEM specimens were prepared from a single crystal of B20-type FeGe using a standard lift-out method from the bulk using a FIB instrument (Helios 5 CX DualBeam, Thermo Fisher Scientific). The FeGe lamellae used in this work had lateral dimensions of the order of a few micrometres in each direction.

In situ optical Lorentz TEM experiments

Fresnel defocus images were recorded in a four-dimensional electron microscopy system based on a Thermo Fisher Talos F200i[26]. Experiments were performed at 95 K using a double-tilt cooling holder (Gatan model 915). Lorentz images were recorded in Fresnel mode with an out-of-plane magnetic field applied to the sample via the objective lens by tuning its current. The defocus distance for all Fresnel defocus Lorentz images was 700 µm.

The experimental set-up allows single-shot femtosecond laser excitation under Lorentz phase imaging conditions. Femtosecond laser pulses (515 nm for 240 fs) were triggered by a digital delay generator, which delivered single shots with fluences ranging from 0 mJ cm^{-2} to 40 mJ cm^{-2}. The laser spot was adjusted to ~50 µm to ensure uniform illumination of the sample. According to a previous report[48], under the present experimental conditions, the optical reflectivity of FeGe was ~47 % and the penetration depth was estimated to be 15.8 nm.

Micromagnetic simulations

In our theoretical examination of magnetic states, we employed a canonical model designed for isotropic chiral magnets. This model encompasses Heisenberg exchange, DMI and demagnetizing fields. The corresponding energy density functional can be expressed as follows[13,49]:

$$\mathcal{E} = \int_{V_m} \mathrm{d}\mathbf{r} \mathcal{A} \sum_{i=x,y,z} |\nabla m_i|^2 + \mathcal{D}\mathbf{m} \cdot (\nabla \times \mathbf{m}) - M_s \mathbf{m} \cdot \mathbf{B} + \frac{1}{2\mu_0} \int_{\mathbb{R}^3} \mathrm{d}\mathbf{r} \sum_{i=x,y,z} |\nabla A_{d,i}|^2, \quad (3)$$

where V_m is the volume of the magnetic sample, $\mathbf{m}(\mathbf{r}) = \mathbf{M}(\mathbf{r})/M_s$ is the magnetization vector field, M_s is the saturation magnetization, μ_0 is the vacuum permeability, $A_d(r)$ is the component of the magnetic vector potential induced by the magnetization, and $\mathcal{A}$ and $\mathcal{D}$ are the Heisenberg exchange constant and DMI constant, respectively. It is assumed that the magnetic field $\mathbf{B}(\mathbf{r})$ is a sum of the external magnetic field $\mathbf{B}_{ext}$ and the demagnetizing field produced by the sample: $\mathbf{B} = \mathbf{B}_{ext} + \nabla \times \mathbf{A}_d$. Here we use material parameters for FeGe: $\mathcal{A} = 4.75$ pJ m^{-1}, $\mathcal{D} = 0.853$ mJ m^{-2} and $M_s = 384$ kA m^{-1}. We define the critical field above which the conical phase transitions to the ferromagnetic state as $B_c = B_D + \mu_0 M_s$, where $B_D = \mathcal{D}^2/(2M_s\mathcal{A})$; the magnetic field is applied perpendicular to the plate. Periodic boundary conditions were applied in the x–y plane. The damaged layer was ~7 nm. All the micromagnetic simulations were performed using Excalibur[50].

Initial state for hopfions

In this section, we outline the procedure for generating an initial hopfion configuration, which serves as a starting point for micromagnetic simulations. We consider a magnetization vector field $\mathbf{m}$ on an $\mathbb{S}^2$ sphere, parameterized by an azimuthal angle Φ and a polar angle Θ, that is, $\mathbf{m} = (\sin\Theta\cos\Phi, \sin\Theta\sin\Phi, \cos\Theta)$. Making use of equations (4) and (5), we embedded a hopfion into a ferromagnetic background[13]:

$$\Theta = \pi\left(1 - \frac{\eta}{R_1}\right), \quad 0 \le \eta \le R_1, \quad (4)$$

$$\Phi = \arctan\left(\frac{y}{x}\right) - \arctan\left(\frac{z}{R_2 - \rho}\right) - \frac{\pi}{2}, \quad (5)$$

where R_1 and R_2 are the minor and major radii of the hopfion, respectively. $\rho = \sqrt{x^2 + y^2}$ and $\eta = \sqrt{(R-\rho)^2 + z^2}$. However, a hopfion created by equations (4) and (5) was found to be unstable in these calculations. To stabilize it, other transformations were performed on this texture.

First, the hopfion was rotated by 90° about the y axis, as shown in Extended Data Fig. 1a. This rotation can be expressed in the form:

$$\mathbf{m}' = \begin{bmatrix} \cos\frac{\pi}{2} & 0 & \sin\frac{\pi}{2} \\ 0 & 1 & 0 \\ -\sin\frac{\pi}{2} & 0 & \cos\frac{\pi}{2} \end{bmatrix} \mathbf{m}. \quad (6)$$

Next, spiralization was applied to the texture in Extended Data Fig. 1a in the $+z$ direction, resulting in the configuration shown in Extended Data Fig. 1b.

By relaxing the state in Extended Data Fig. 1b, a hopfion embedded in a cone state was obtained, as shown in Extended Data Fig. 1c. This configuration agrees well with our experimental observations. The spiralization along the z direction can be expressed in the form:

$$\mathbf{m}'' = \begin{bmatrix} \cos\varphi & -\sin\varphi & 0 \\ \sin\varphi & \cos\varphi & 0 \\ 0 & 0 & 1 \end{bmatrix} \mathbf{m}', \quad \varphi = \frac{2\pi}{L_D} z. \quad (7)$$

After energy minimization (relaxation) of the initial configuration, the texture shown in Fig. 1a and Extended Data Fig. 1c was obtained. In Extended Data Fig. 1c, the hopfion is visualized via the isosurface at $m_x = 0$, whereas in Fig. 1a, the isosurface for $m_z < 0$ is displayed. An alternative way to visualize a hopfion embedded in a helical background is through despiralization—the opposite procedure to spiralization—defined by $\varphi' = -\varphi$. When it is applied to the texture shown in Extended Data Fig. 1c, this transformation yields a hopfion embedded in a ferromagnetic background, as illustrated in Extended Data Fig. 1d.

Hopfion stability diagram

The stability diagram shown in Fig. 4a was calculated using Excalibur with the following parameters. The cuboid size in the finite difference scheme was fixed at 1.75 nm × 1.75 nm × 1.75 nm. To suppress interactions between periodic images of the hopfion resulting from the boundary conditions in the x–y plane, a relatively large simulation domain of 560 nm × 560 nm (320 cuboids in each lateral direction) was used. The sample thickness was defined by the number of cuboid layers along the z axis.

For each sample thickness, the stability of the hopfion was tested by starting in zero field and gradually increasing the applied magnetic field $\mathbf{B}_{ext} \parallel \mathbf{e}_z$, where $\mathbf{e}_z$ is the unit vector along the z direction, until the hopfion collapsed. Calculations were performed both with and without the presence of a FIB-damaged layer, which was modelled as four cuboid layers (~7 nm) at each sample surface.

MEP calculations

To compute the MEPs shown in Fig. 5, the regularized geodesic nudged elastic band (RGNEB) method[51] was used. RGNEB extends the standard GNEB approach[45,46] to the regularized micromagnetic model introduced in ref. 52. In the regularized micromagnetic model, the order parameter is a four-dimensional vector $\mathbf{v} = (v_1, v_2, v_3, v_4)$ constrained to the $\mathbb{S}^3$ sphere, so that $|\mathbf{v}| = 1$. The first three components correspond to the magnetization $\mathbf{m} = (m_x, m_y, m_z)$, whereas the fourth, auxiliary component satisfies $v_4^2 = 1 - |\mathbf{m}|^2$. This representation imposes the natural constraint $|\mathbf{m}| \le 1$ across the entire sample. Within this model, the Heisenberg exchange term in equation (3) is replaced by

$$\mathcal{A} \sum_{i=x,y,z} |\nabla m_i|^2 \mapsto \mathcal{A} \sum_{i=1}^{4} |\nabla v_i|^2 + \kappa v_4^2, \quad (8)$$

where κ is a phenomenological constant (J m^{-3}) that determines the Bloch point localization[52]. All the other terms in the micromagnetic Hamiltonian follow from the substitution $(m_x, m_y, m_z) \mapsto (v_1, v_2, v_3)$ and are independent of v_4.

RGNEB calculations were performed using an open-source micromagnetic simulation package[53] that is based on a fork of the MuMax3 code[54]. The material parameters were identical to those used in micromagnetic simulations, with $\kappa = 10^{-3} M_s B_D$ (≈ 76.54 J m^{-3}). As shown earlier in ref. 51, for $10^{-4} < \kappa/M_s B_D < 10^{-2}$, the energy barrier varies negligibly. The calculations were performed in a domain with sizes in the x and y directions of 210 nm and a thickness of 105 nm. The mesh density was $128 \times 128 \times 64$ nodes. For consistency with the micromagnetic simulations, in the MEP calculations, periodic boundary conditions were applied in the x–y plane and a FIB-damaged layer of thickness ~7 nm was assumed on each sample surface. The reaction coordinates in the MEP calculations shown in Fig. 5a and Extended Data Fig. 9a–c are given in reduced units.

The MEP shown in Fig. 5 comprises three segments that connect local energy minima representing a skyrmion–antiskyrmion pair, a hopfion and a conical state with weak surface modulations. Snapshots of the skyrmion–antiskyrmion pair and hopfion are shown in Fig. 5b,e, respectively. More snapshots of intermediate states along each MEP are provided in Extended Data Fig. 9. Initial paths were constructed using snapshots of the system obtained during micromagnetic simulations of corresponding processes[55]. For example, to generate an initial path describing a skyrmion–antiskyrmion merger into a hopfion, a skyrmion and an antiskyrmion were placed at a distance at which they begin to merge under energy minimization. Intermediate snapshots of this evolution were then used as images forming the initial guess for the MEP calculation. These pseudo-dynamical simulations were performed using the Excalibur code[50]. The final MEPs were obtained using an iterative RGNEB algorithm.

Homotopy group derivation

In this section, we use algebraic topology, focusing on the long exact sequence of homotopy groups, $\pi_i(A)$ and $\pi_j(B)$, and relative homotopy groups, $\pi_k(A, B)$, for the pair of spaces $A \supseteq B$. The sequence is a chain of group homomorphisms, such that the image of one homomorphism equals the kernel of the next[35]. We derive group $G \equiv \pi_3(A, B)$ based on other groups surrounding it in the chain. The third relative homotopy group π_3 is a homotopy group classifying maps introduced in equation (1), so that the domain for the function f is the cube I^3 and the overall codomain is the set A, $f(\mathbf{r} \in I^3) \in A$. On the boundary of the cube, the function takes values in B, $f(\mathbf{r} \in \partial I^3) \in B$. For our order parameter, the space is the sphere $A = \mathbb{S}^2$, and the subspace is associated with restrictions on this sphere, so we denote it by the set-theoretic difference $B = \mathbb{S}^2 \backslash \bigcup_{i=1}^{n} X_i$. Each X_i in the above union is either a point on the sphere or a contractible region (such as a spherical cap) with or without a boundary. Also, none of these domains overlap, $X_i \cap X_{j \neq i} = \varnothing$. The total number of punctured domains (holes) is any positive integer, $n \in \mathbb{Z}^+$. For every such B, there is a deformation retraction of B into some connected graph Γ. This mapping can be thought of as expanding every hole X_i so that, at the end, all that remains from the sphere is a set of lines connected by points. Thus, we have homotopy equivalence, $B \simeq \Gamma$. In turn, the higher homotopy groups of a connected graph are trivial, $\pi_{i \geq 2}(\Gamma) = 0$, which can be revealed, for example, by taking the tree (it is a contractible space) as the universal cover of the graph[35]. The last important component here is the classic result of homotopy theory established by Hopf et al.: the third homotopy group of the sphere is isomorphic to the integers, $\pi_3(\mathbb{S}^2) = \mathbb{Z}$.

Substituting all the above equalities into the long exact sequence, we obtain:

$$\begin{array}{ccccccccccc} \ldots & \to & \pi_3(B) & \to & \pi_3(A) & \to & \pi_3(A,B) & \to & \pi_2(B) & \to & \ldots \\ & & \| & & \| & & \| & & \| & & \\ \ldots & \longrightarrow & 0 & \longrightarrow & \mathbb{Z} & \longrightarrow & G & \longrightarrow & 0 & \longrightarrow & \ldots \end{array} \tag{9}$$

In the resulting short exact sequence (chain of three homomorphisms bounded by zeros), the central homomorphism can only be an isomorphism. Therefore:

$$G = \mathbb{Z}, \tag{10}$$

which completes the derivation of equation (2) presented in the main text.

Below, we provide some important special cases of equation (2) in full notation:

$$\pi_3(\mathbb{S}^2, \mathbb{S}^2 \backslash \{P_1\}) = \pi_3(\mathbb{S}^2, P_0) \equiv \pi_3(\mathbb{S}^2) = \mathbb{Z}, \tag{11}$$

$$\pi_3(\mathbb{S}^2, \mathbb{S}^2 \backslash \{P_1, P_2\}) = \pi_3(\mathbb{S}^2, \mathbb{S}^1) = \mathbb{Z}, \tag{12}$$

$$\pi_3(\mathbb{S}^2, \mathbb{S}^2 \backslash \{P_1, P_2, P_3\}) = \pi_3(\mathbb{S}^2, \mathbb{S}^1 \vee \mathbb{S}^1) = \mathbb{Z}, \tag{13}$$

where P_i are points on the sphere.

Hopf index calculation

Our method of finding the integer topological invariant H for equation (2) involves a two-step procedure. First, we apply an auxiliary map $p : \mathbf{m}(\mathbf{r}) \mapsto \mathfrak{m}(\mathbf{r})$, such that it does not change the topological invariant H but simplifies the boundary conditions: $\mathfrak{m}(\mathbf{r} \in \partial\Omega) = \text{const}$, where Ω denotes the domain of hopfion localization and $\partial\Omega$ is the boundary of this domain. Second, we use the Whitehead integral formula.

We focus on the case isolated in equation (11) and then prove that the same routine is universal for all other cases of equation (2). For the auxiliary map, we use deformation retraction resembling the half of the 'dumbbell' introduced in ref. 41. For convenience and without loss of generality, we assume that the base point is the north pole (P_N), and the punctured point is the south pole (P_S):

$$p : (\mathbb{S}^2, \mathbb{S}^2 \backslash \{P_S\}) \to (\mathbb{S}^2, P_N), \tag{14}$$

$$\begin{pmatrix} m_x \\ m_y \\ m_z \end{pmatrix} \mapsto \begin{pmatrix} 2\gamma m_x \\ 2\gamma m_y \\ 1 - 2\gamma^2(1 - m_z)(1 + \mu) \end{pmatrix}, \tag{15}$$

where

$$\gamma = \begin{cases} \sqrt{\frac{\mu - m_z}{(1 - m_z)(1 + \mu)^2}}, & \text{if } m_z < \mu, \\ 0, & \text{otherwise,} \end{cases}$$

and where the parameter $\mu = \mu(\mathbf{r})$ is a monotone function that changes in value from +1 to −1 from inside Ω to the boundary $\partial\Omega$. For Ω in the form of a cuboid described in dimensionless coordinates as $r_{1,2,3} \in [-1/2, 1/2]$, we use

$$\mu(\mathbf{r}) = 128\left(\frac{1}{4} - r_1^2\right)\left(\frac{1}{4} - r_2^2\right)\left(\frac{1}{4} - r_3^2\right) - 1. \tag{16}$$

For the unit vector field $\mathfrak{m}$ obtained from equation (15), we calculate the Whitehead integral:

$$H = -\frac{1}{16\pi^2} \int_{\Omega} \mathrm{d}\mathbf{r}\, \mathbf{F} \cdot [(\nabla\times)^{-1}\mathbf{F}], \tag{17}$$

where $\mathbf{F}$ represents the vector of curvature, defined as

$$\mathbf{F} \equiv \begin{pmatrix} \mathfrak{m} \cdot [\partial_{r_2}\mathfrak{m} \times \partial_{r_3}\mathfrak{m}] \\ \mathfrak{m} \cdot [\partial_{r_3}\mathfrak{m} \times \partial_{r_1}\mathfrak{m}] \\ \mathfrak{m} \cdot [\partial_{r_1}\mathfrak{m} \times \partial_{r_2}\mathfrak{m}] \end{pmatrix}. \tag{18}$$

As in ref. 13, the vector field **F** was calculated using the Berg–Lüscher method[56], and the following integral was calculated numerically to give the vector potential:

$$(\nabla\times)^{-1}\mathbf{F} = \int_{-1/2}^{r_1} \mathrm{d}r_1\, \mathbf{F}\times\hat{\mathbf{e}}_{r_1}. \tag{19}$$

Next, we prove that the procedure starting with equation (15) is universal for all other cases. Because every holey sphere can be considered as an inclusion into the single-punctured sphere,

$$\mathbb{S}^2\backslash \bigcup_{i=1}^{n} X_i \hookrightarrow \mathbb{S}^2\backslash\{P_j\} \tag{20}$$

there is an induced homomorphism of the corresponding relative homotopy groups:

$$\begin{array}{ccc} \pi_3(\mathbb{S}^2, \mathbb{S}^2\backslash\bigcup_{i=1}^{n} X_i) & \to & \pi_3(\mathbb{S}^2, \mathbb{S}^2\backslash\{P_j\}) \\ \| & & \| \\ \mathbb{Z} & \longrightarrow & \mathbb{Z} \end{array}. \tag{21}$$

A simple analysis reveals that homomorphism equation (21) is an isomorphism. Indeed, an arbitrary element $\mathfrak{m}_k$ of the group $\pi_3(\mathbb{S}^2)$ is an element of both groups in equation (21) because one can always choose a base point outside the holes. Let us consider one of these elements that has unit charge, $H(\mathfrak{m}_k) = 1$. It turns out that a homomorphism from integers to integers (endomorphism[57]), which is always multiplication by an integer, can result in an integer equal to 1. This is possible only if the homomorphism is a multiplication by ±1. As such multiplications are in the group of automorphisms $\mathrm{Aut}(\mathbb{Z})$, we obtain that the homomorphism equation (21) is an isomorphism. Accordingly, to calculate H, the procedure starting with equation (15) is always applied when choosing a base point outside the holes.

Data availability

All data are available from the corresponding authors upon reasonable request. Source data are provided with this paper.

Code availability

All simulations were performed using established commercial or publicly available software. All source codes are available from the corresponding authors upon reasonable request.

References

48. Guritanu, V. et al. Optical evidence for heavy charge carriers in FeGe. *Phys. Rev. B* **75**, 155114 (2007).
49. Savchenko, A. S. et al. Diversity of states in a chiral magnet nanocylinder. *APL Mater.* **10**, 061110 (2022).
50. Rybakov, F. N. & Babaev, E. *Excalibur Software* http://quantum-andclassical.com/excalibur/ (Quantum and Classical Solutions).
51. Kuchkin, V. M. et al. Stability and nucleation of dipole strings in uniaxial chiral magnets. *Phys. Rev. B* **111**, 174410 (2025).
52. Kuchkin, V. M. et al. Quantum and classical magnetic Bloch points. *Phys. Rev. Res.* **7**, 013195 (2025).
53. Kuchkin, V. M. Regularized LLG simulations MuMax3 (extension). *GitHub* http://github.com/kuchkin/mumax3-gneb (2023).
54. Vansteenkiste, A. et al. The design and verification of MuMax3. *AIP Adv.* **4**, 107133 (2014).
55. Kuchkin, V. M. & Kiselev, N. S. Homotopy transitions and 3D magnetic solitons. *APL Mater.* **10**, 071102 (2022).
56. Berg, B. & Lüscher, M. Definition and statistical distributions of a topological number in the lattice $O(3)\sigma$-model. *Nucl. Phys. B* **190**, 412–424 (1981).
57. Rotman, J. J. *An Introduction to the Theory of Groups* (Springer, 1995).

Acknowledgements

X.C., D.Y. and F.Z. acknowledge financial support from the National Natural Science Fund (Grant Nos. 92477130, 12127803, 12427806 and 52373226), the Excellent Young Scientists Fund Program (Overseas), the National Key R&D Program of China (Grant Nos. 2024YFA1611100, 2020YFA0309300 and 2024YFA1408000) and the Fundamental Research Funds for the Central Universities. F.Z. is grateful to the GJYC programme of Guangzhou (Grant No. 2024D01J0060), the Guangzhou Basic and Applied Basic Research Foundation (Grant No. SL2024A04J00852), the Guangdong Provincial Quantum Science Strategic Initiative (Grant No. GDZX2401002) and the Xiaomi Young Talents Program. V.M.K. acknowledges financial support from the European Union's Horizon Europe research and innovation programme under a Marie Skłodowska-Curie grant (Agreement No. 101203692, QUANTHOPF). N.S.K. acknowledges financial support from the European Research Council under the European Union's Horizon 2020 research and innovation programme (Grant No. 856538 for Project '3D MAGiC'). F.N.R. and O.E. acknowledge support from the Swedish Research Council (Grant No. 2023-04899). R.E.D.-B. is grateful for financial support from the Deutsche Forschungsgemeinschaft (Project ID 405553726, TRR 270).

Author contributions

F.Z. initialized the concept. F.Z. and X.F. conceived the project and designed the experiments. H.Z. synthesized the FeGe crystals. X.C. prepared the TEM samples. X.C. performed the experiments and data analysis under the supervision of X.F. and F.Z. D.Y. and N.S.K. performed the micromagnetic simulations and analysed the theoretical TEM images. A.S.S. calculated the phase diagram. V.M.K. performed the MEP calculations. F.N.R. developed the homotopy group theory. X.C., N.S.K., F.N.R. and F.Z. prepared the paper. All authors discussed the results and contributed to the final article.

Funding

Open access funding provided by Forschungszentrum Jülich GmbH.

Competing interests

The authors declare no competing interests.

Additional information

Extended data is available for this paper at https://doi.org/10.1038/s41567-026-03236-0.

Supplementary information The online version contains supplementary material available at https://doi.org/10.1038/s41567-026-03236-0.

Correspondence and requests for materials should be addressed to Filipp N. Rybakov, Nikolai S. Kiselev, Xuewen Fu or Fengshan Zheng.

Peer review information *Nature Physics* thanks the anonymous reviewers for their contribution to the peer review of this work. Peer reviewer reports are available.

https://doi.org/10.1038/s41567-026-03236-0

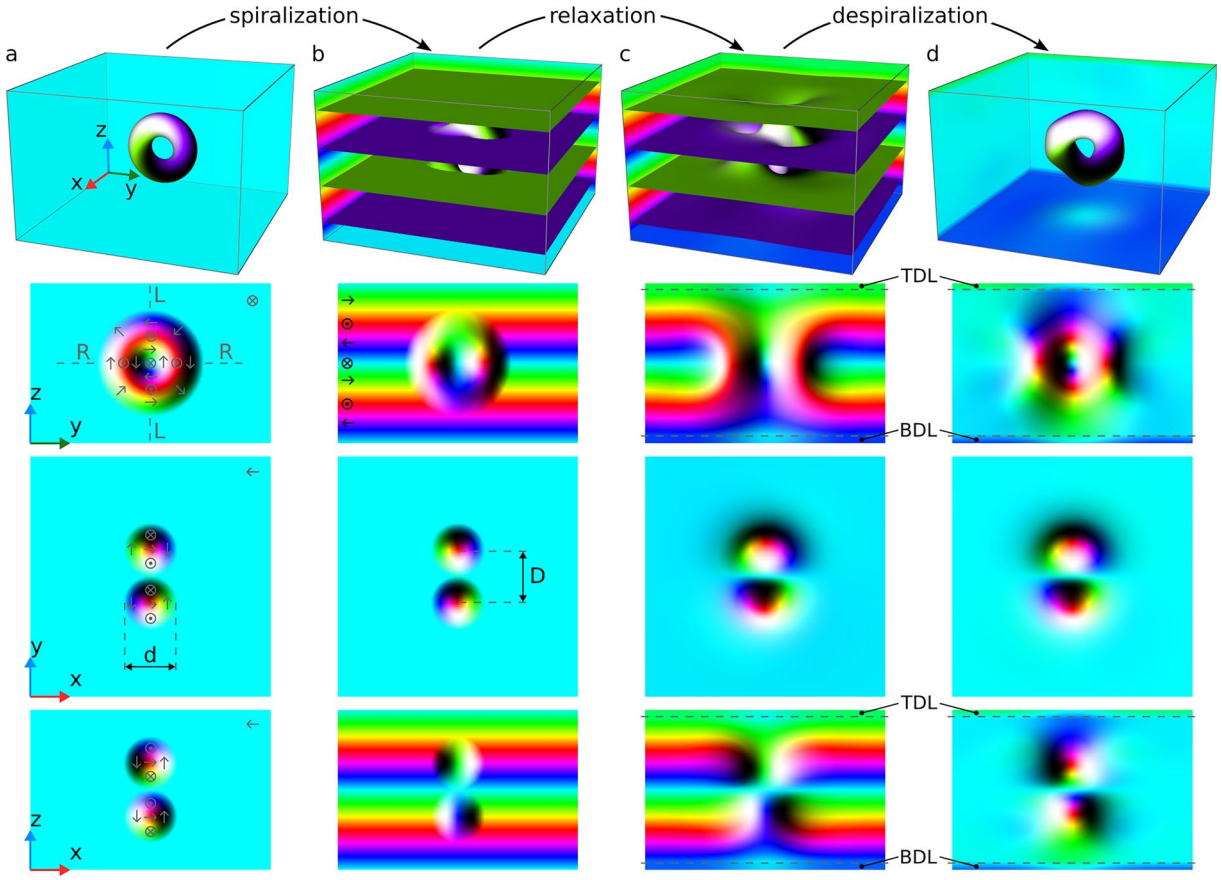

Extended Data Fig. 1 | Spin texture in a simulated box of size $4L_D \times 4L_D \times 2L_D$, with $L_D = 70$ nm. a, The first column shows the initial hopfion ansatz embedded in a ferromagnetic background with $m_0 = (-1, 0, 0)$. **b**, The second column shows the spin texture after applying the spiralization Eq. (7), where the spiral's wavevector k is parallel to the z axis with $|k| = 2\pi/L_D$. **c**, The third column shows the spin texture following energy minimization, assuming periodic boundary condition in the xy plane. **d**, The fourth column shows the relaxed spin texture from **c** after applying despiralization. The first row shows isosurfaces of $m_x = 0$. The second, third, and fourth rows show the magnetization field in the y-z, x-y, and x-z middle planes, respectively. The parameters d and D define the small and large diameters of the toroidal hopfion ansatz. In the configuration shown in **a**, $d = D = 0.3L_D$. The grid size is $140 \times 140 \times 70$. Color mapping: Black: magnetic moments aligned along the $+z$ direction; Green: magnetic moments aligned along the $+y$ direction; Red: magnetic moments aligned along the $+x$ direction.

https://doi.org/10.1038/s41567-026-03236-0

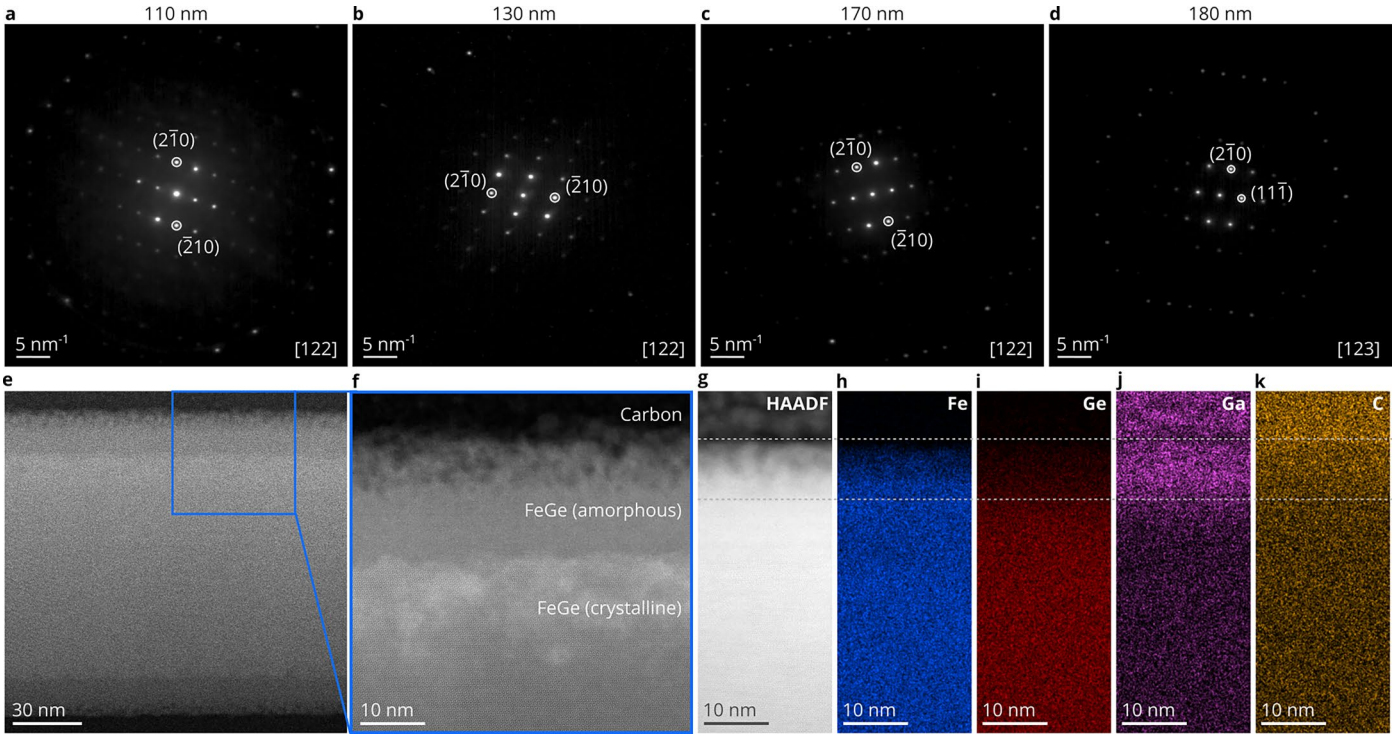

Extended Data Fig. 2 | Diffraction patterns and cross-sectional TEM analysis. **a**–**c**, Diffraction patterns recorded from 110nm-thick-, 130-nm-thick, and 170-nm-thick FeGe samples, with the zone axis [122] oriented along the plate normal. **d**, Diffraction pattern recorded from a 180-nm-thick FeGe sample with the zone axis [123] oriented along the plate normal. **e**, Cross-sectional high-angle annular dark field (HAADF) image of a FIB-prepared FeGe lamella recorded in scanning TEM (STEM) mode. The FeGe sample was first thinned to approximately 150 nm using FIB milling. Carbon protective layers were deposited on both sides of the lamella plane, after which a cross-sectional specimen was extracted and mounted on a FIB lift-out grid. Final thinning was performed using plasma FIB (Helios 5 Hydra UX DualBeam, Thermo Fisher Scientific) to avoid secondary Ga^+ implantation. The image reveals a crystalline FeGe layer (100-nm-thick) sandwiched between FIB-induced amorphous FeGe layers. **f**, Magnified view of the interface between the amorphous and crystalline FeGe layers. **g**–**k**, Energy dispersive X-ray elemental maps showing Ga^+ implantation into the FeGe lamella, with an estimated penetration depth of ~ 8 ± 2 nm defining the damaged region where Ge is removed.

https://doi.org/10.1038/s41567-026-03236-0

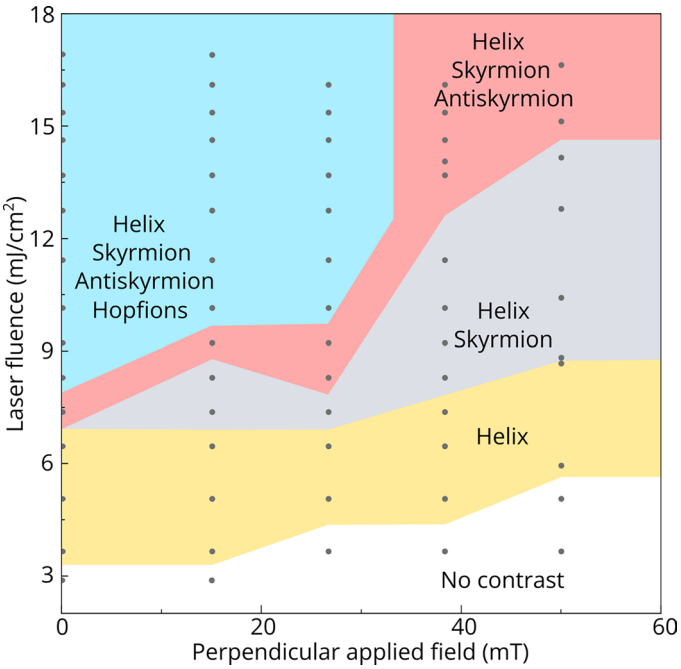

Extended Data Fig. 3 | Experimental data points in a phase diagram for a 110-nm-thick FeGe plate. These data points were used to construct the schematic phase diagram shown in Fig. 1b. Each gray point corresponds to a specific value of the applied magnetic field (0–50 mT) and laser fluence (0–17 mJ/cm^2). Before each measurement, the sample was taken to magnetic saturation in a positive out-of-plane field. Laser pulses were then repeatedly applied at a frequency of 1 Hz, typically at least 50 times, to statistically assess the presence or absence of a particular spin texture. If the Lorentz TEM contrast characteristic of the corresponding magnetic texture (helix, skyrmion, antiskyrmion, hopfion) was observed in at least one measurement, then the data point was assigned to the corresponding domain in the diagram.

https://doi.org/10.1038/s41567-026-03236-0

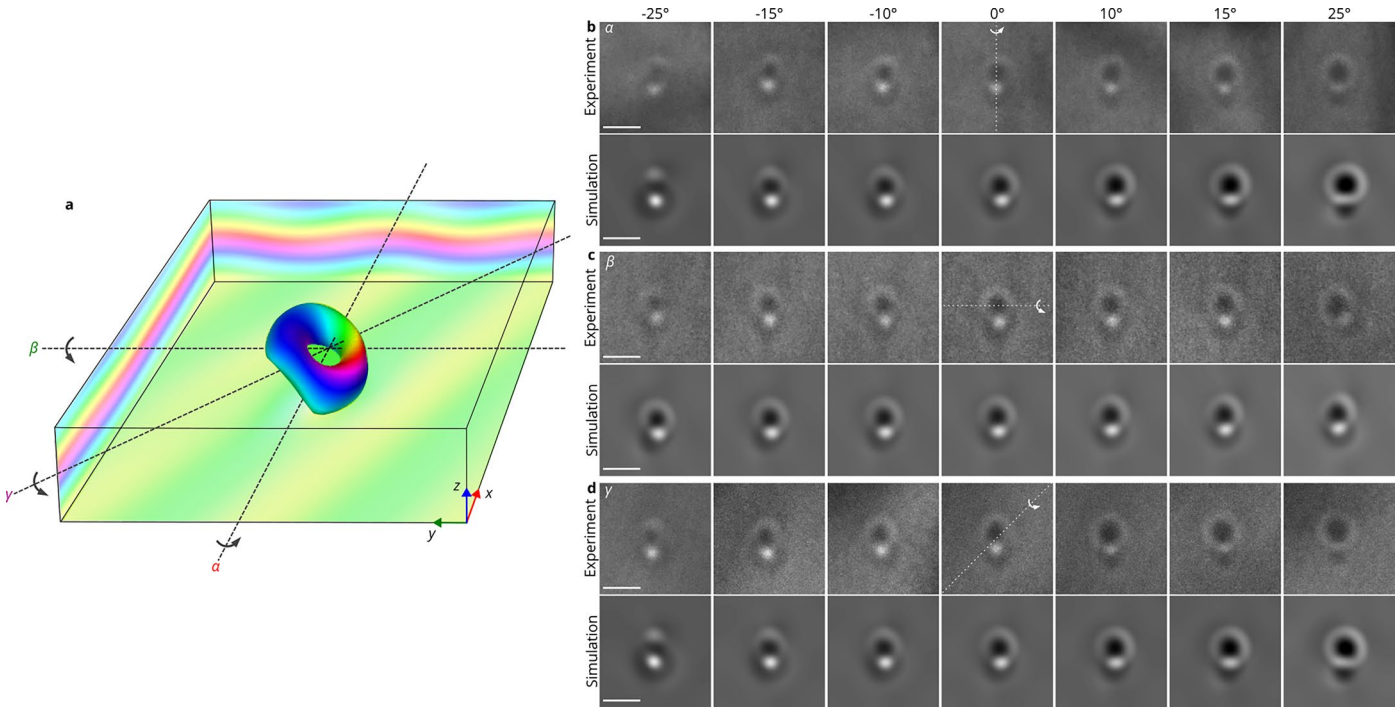

Extended Data Fig. 4 | Tilt series of Lorentz TEM images of hopfions. **a**, Three-dimensional isosurface of a hopfion. The labeled axes indicate rotation directions for the tilt series. **b**, Tilt series of over-focus Lorentz TEM images of the hopfion rotated around the α axis. **c**, Tilt series of over-focus Lorentz TEM images of the hopfion rotated around the β axis. **d**, Tilt series of over-focus Lorentz TEM images of the hopfion rotated around the γ axis. Upper panel: Experimental over-focus Lorentz TEM images; lower panel: Corresponding simulated over-focus Lorentz TEM images. The rotation angles are labeled in the upper panel. The Lorentz TEM images were recorded at 95 K with a defocus value of 700 μm. The sample thickness is 110 nm in panels **b** and **c**, and 130 nm in panel **d**. The simulations in panels **b** and **c** were performed in domains of identical size (300 nm × 300 nm × 110 nm), while those in panel d used a domain of 300 nm × 300 nm × 130 nm. The scale bar is 100 nm.

https://doi.org/10.1038/s41567-026-03236-0

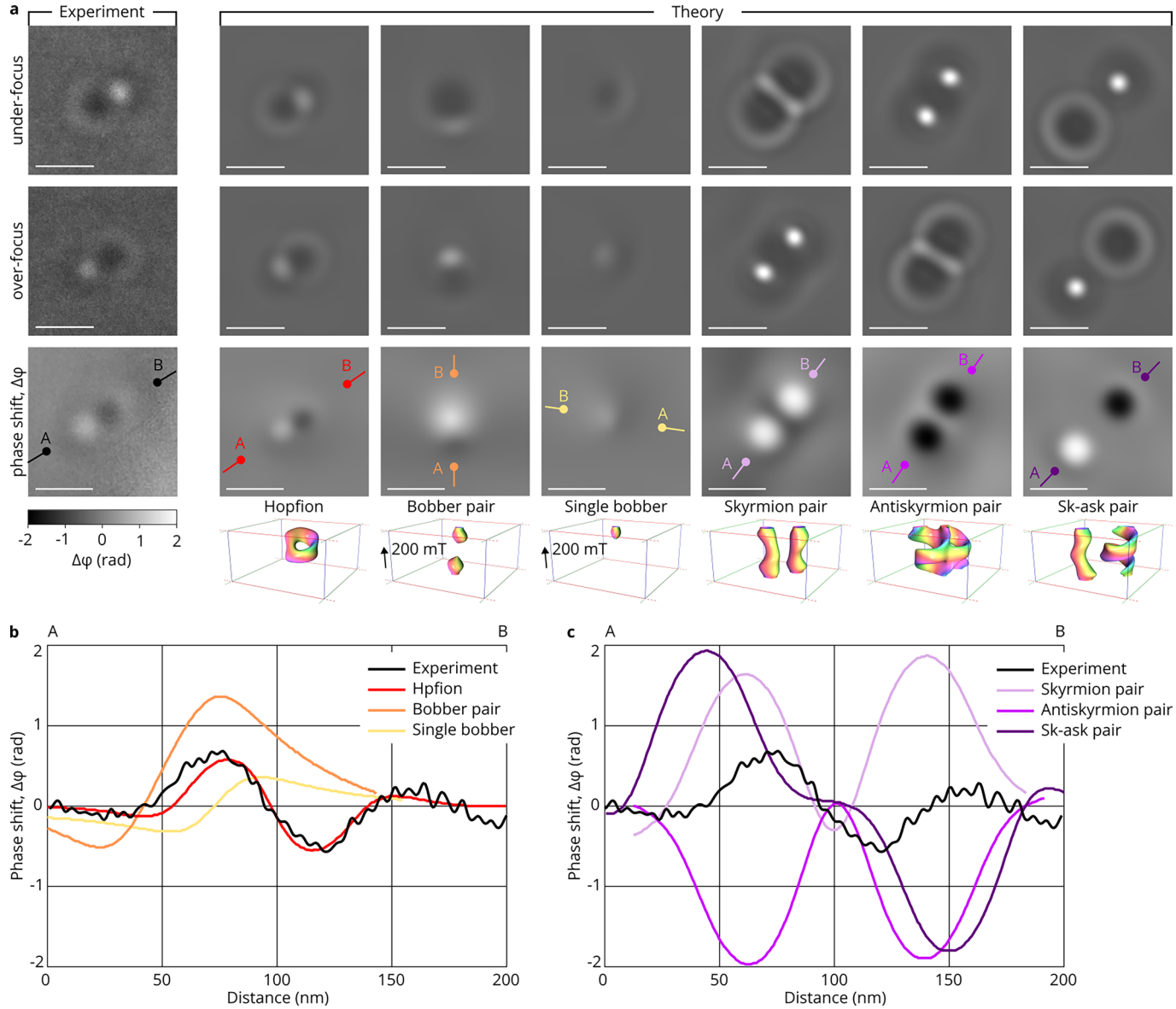

Extended Data Fig. 5 | Quantitative comparison between experimental and theoretical TEM images for different statically stable configurations. The first column in **a** shows experimental Lorentz TEM images recorded from a 130-nm-thick sample at 95 K in zero applied magnetic field. The remaining columns in **a** show simulated Lorentz TEM contrast for different statically stable magnetic configurations, illustrated at the bottom of each column by an isosurface of $m_z = -0.45$. All of the simulations were performed in domains of identical size (256 nm × 256 nm × 130 nm) using the same material parameters (see Methods) and including a 7-nm-thick dead layer at the sample surfaces. All of the configurations correspond to local energy minima in zero magnetic field, except for chiral bobbers, which require an external magnetic field for stability. The first and second rows in a show under-focus and over-focus Lorentz TEM images, respectively. The defocus distance is identical for the experimental images and simulations and equals 700 μm. The scale bar in all images in a is 100 nm. The third row show electron phase shift maps, which were recorded using off-axis electron holography and, unlike Lorentz TEM, provide a quantitative signal. All of the experimental and simulated phase shift images are shown on the same gray scale, as indicated at the bottom of the first column. Panels **b** and **c** compare line profiles extracted from the phase shift maps in **a** along the lines connecting points A and B. The best agreement with the experimental signal is obtained for the hopfion configuration. Other configurations differ in the magnitude and shape of the phase shift profiles and in the stability conditions under which they exist. (Notably, chiral bobbers require an external magnetic field).

https://doi.org/10.1038/s41567-026-03236-0

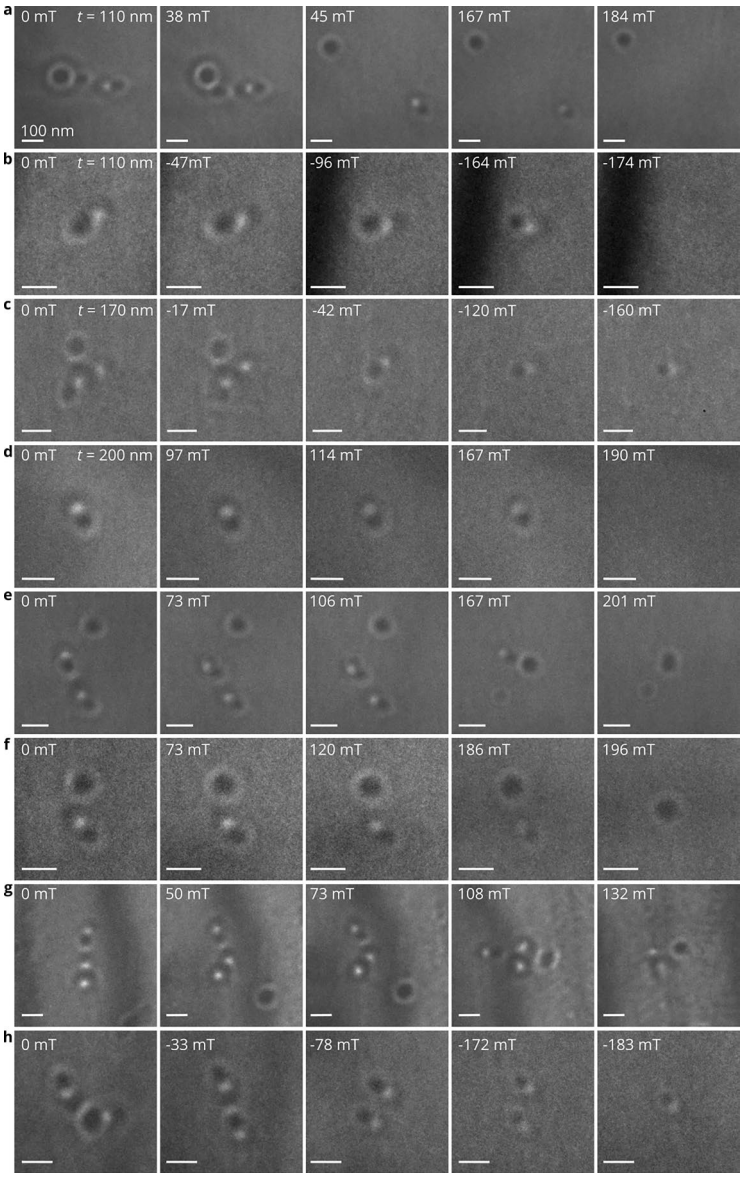

Extended Data Fig. 6 | Under-focus Lorentz TEM images corresponding to the over-focus images shown in Fig. 4 and Fig. 6. a-d correspond to the over-focus images in Fig. 4b-e. **e-h** correspond to the overfocus images in Fig. 6. All of the images were recorded at 95 K with a defocus of 700 µm. The scale bar is 100 nm.

https://doi.org/10.1038/s41567-026-03236-0

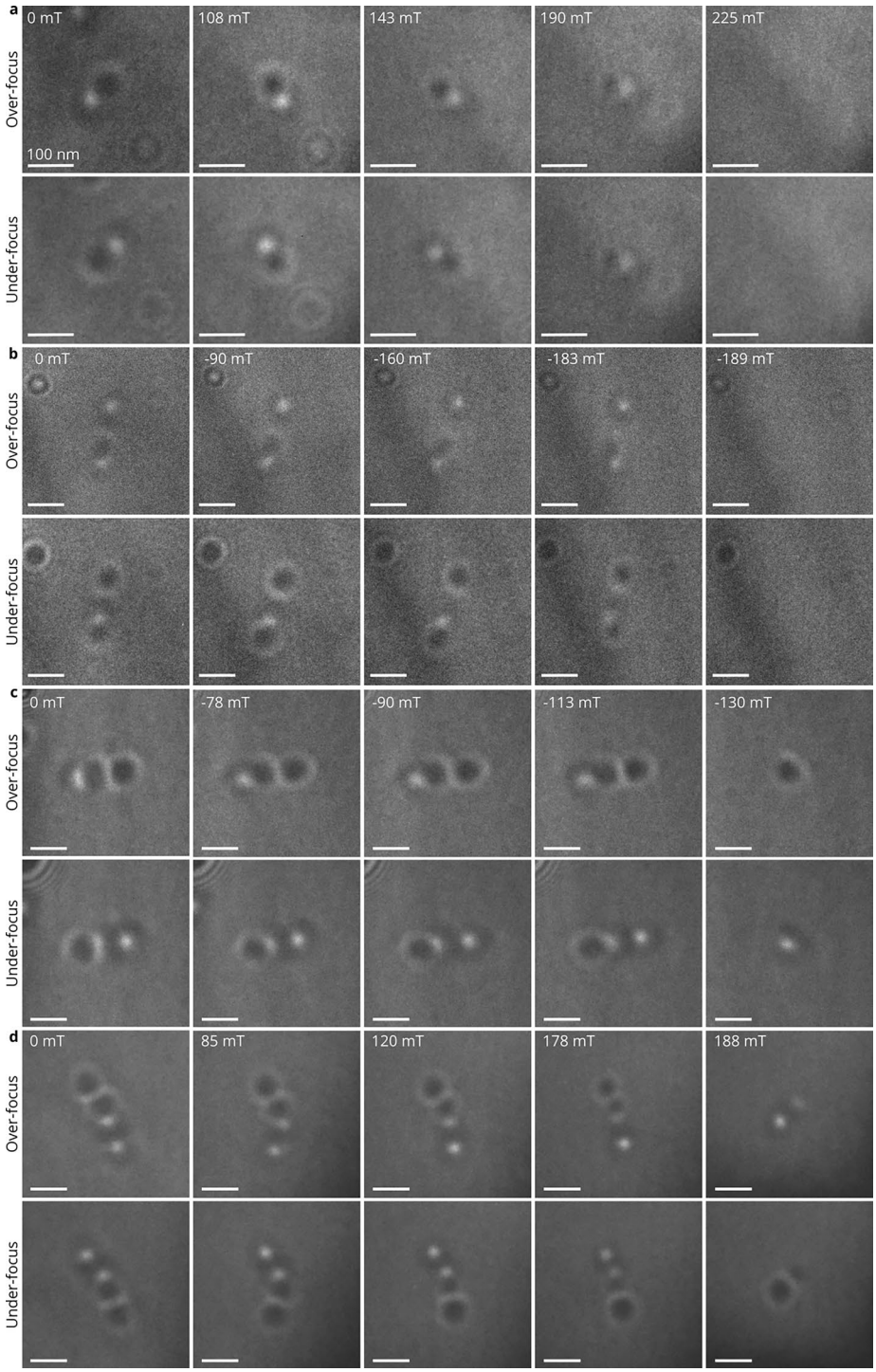

Extended Data Fig. 7 | Field evolution of hopfions in a perpendicular external magnetic field in a 110-nm thick sample. a, Isolated hopfion. **b**, Hopfion-skyrmion. **c**, Hopfion-antiskyrmion. **d**, Hopfion-skyrmion-antiskyrmion. The magnetic field magnitudes are indicated in the upper left corner of each image. All of the images were acquired at 95 K with a defocus value of 700 µm. The scale bar is 100 nm.

https://doi.org/10.1038/s41567-026-03236-0

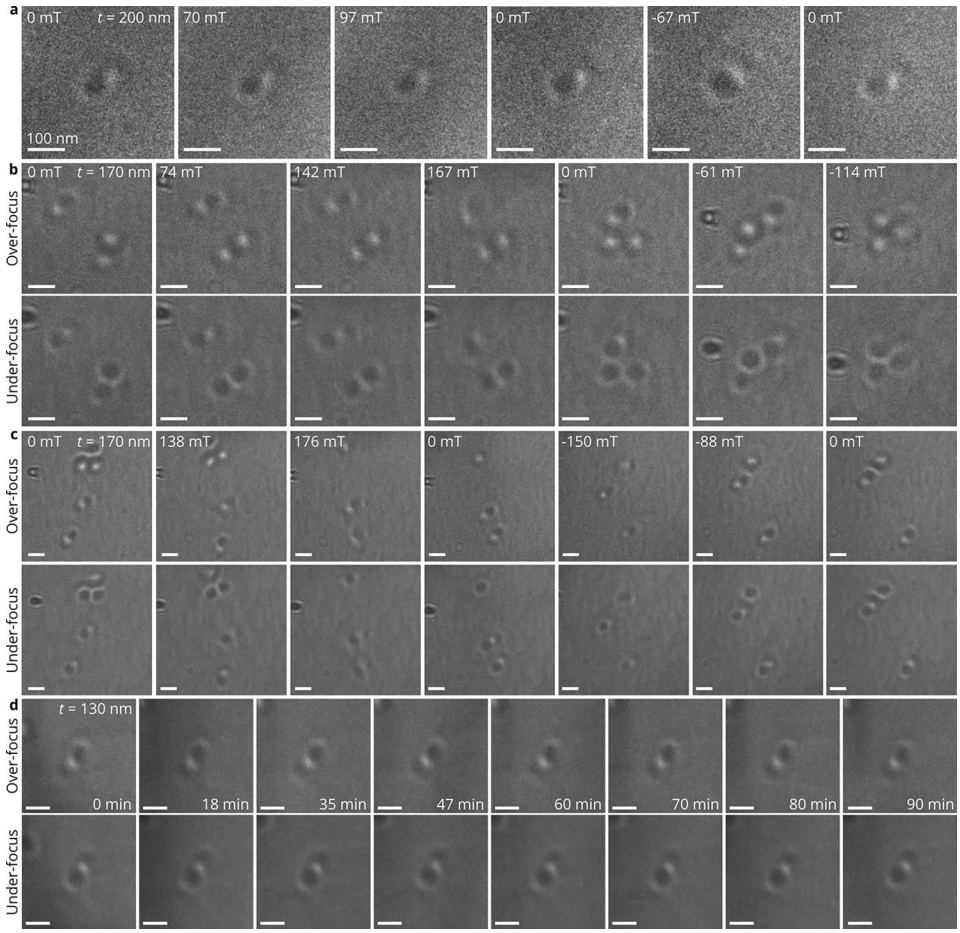

Extended Data Fig. 8 | Field evolution of hopfions in a perpendicular magnetic field in samples of different thickness and temporal stability of an isolated hopfion. a, Field evolution of an isolated hopfion in a 200-nm-thick sample. **b** and **c**, Field evolution of isolated hopfions in a 170-nm-thick sample. The magnetic field magnitudes are indicated in the upper left corners of panels **a**-**c**. **d**, Temporal stability of an isolated hopfion in zero magnetic field in a 130-nm-thick sample. The Lorentz images were acquired at different time points, with the time labeled at the lower right corner. The sample thicknesses are indicated in the upper right corners of the leftmost images. The over-focus Lorentz TEM images were acquired at 95 K with a defocus value of 700 μm. The scale bar is 100 nm.

https://doi.org/10.1038/s41567-026-03236-0

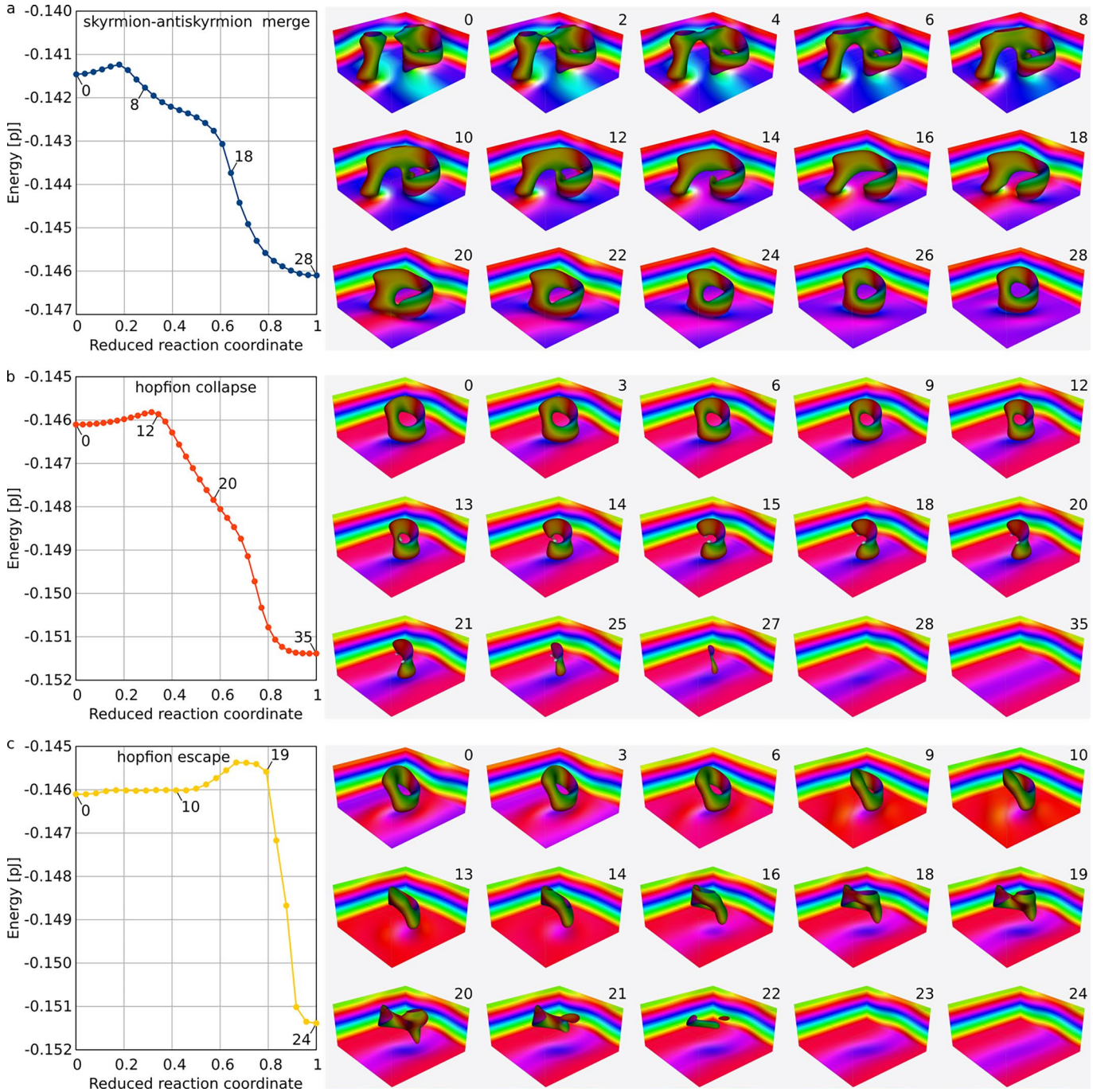

Extended Data Fig. 9 | Extended version of Fig. 5 in the main text. The left panels in **a**, **b**, and **c** show minimum energy paths (MEPs), while the right panels show representative system snapshots at selected points along these paths.

https://doi.org/10.1038/s41567-026-03236-0

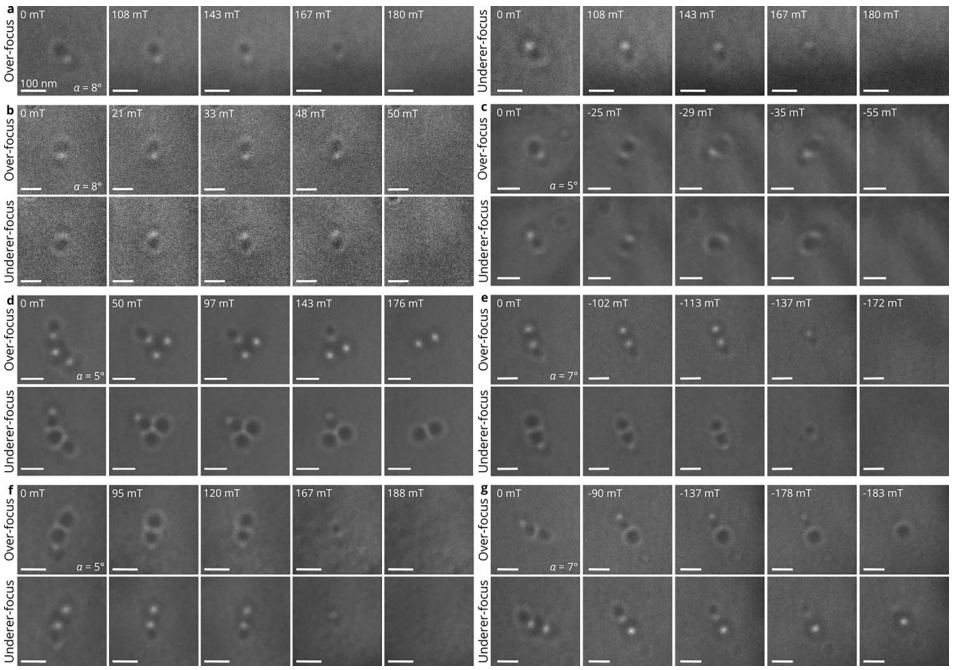

Extended Data Fig. 10 | Field evolution of hopfions in a tilted magnetic field in a 110-nm-thick sample. a-**c**, Isolated hopfions. **d** and **e**, Hopfion-skyrmion pairs. **f** and **g**, Hopfion-antiskyrmion pairs. Panels **a**, **b**, **d** and **f** are for increasing positive fields, while panels **c**, **e**, and **g** are for increasing reversed (negative) fields. An in-plane field component was introduced by tilting the sample to angle α. The strength of the magnetic field is marked in the upper left corner of each image. The Lorentz TEM images were acquired at 95 K with a defocus of 700 µm. The scale bar is 100 nm.